Performance Analysis and Power Allocation for Cooperative ISAC Networks

Meng Liu, *Student Member, IEEE,* Minglei Yang, *Member, IEEE,* Huifang Li, Kun Zeng, *Member, IEEE,* Zhaoming Zhang, Arumugam Nallanathan, *Fellow, IEEE,* Guangjian Wang, *Member, IEEE,* and Lajos Hanzo, *Life Fellow, IEEE*

***Abstract*—To mitigate the overlapping of the radar and communication frequency bands caused by large-scale devices access, we propose a novel integrated sensing and communication (ISAC) system, where a micro base station (MiBS) simultaneously carries out both target sensing and cooperative communication. Concretely, the MiBS, acting as the sensing equipment, can also serve as a full-duplex decode-and-forward relay to assist end-to-end communication. Moreover, non-orthogonal downlink transmission (NO-DLT) is adopted between the macro base station and the Internet-of-Things devices, so that the spectrum utilization can be further improved. To facilitate the performance evaluation, both the exact and asymptotic outage probabilities, the ergodic rates associated communication, and the probability of successful sensing detection are characterized. Subsequently, a pair of problems of maximizing the receive signal-to-interference-plus-noise ratio of the sensing signal and maximizing the sum rate of communication are formulated that are solved by the classic Lagrangian method while exploiting the associated function monotonicity. Our simulation results demonstrate that: 1) The proposed ISAC NO-DLT system improves both the communication and sensing performance under the same power consumption as non-cooperative NO-DLT; 2) The proposed power allocation (PA) schemes are superior to the random PA scheme.**

***Index Terms*—Integrated sensing and communication, cooperative communication, non-orthogonal downlink transmission, full-duplex.**

I. Introduction

A. Background

TRIGGERED by the roll-out of the Internet-of-Things (IoT), a large number of devices are connected to the mobile communication networks, resulting in escalating spectrum demand in support of superior user experience [1]–[3]. In order to alleviate the potential spectrum congestion, diverse methods have been proposed, among which the sensing-communication coexistence (SCC) [4] and the integrated sensing and communication (ISAC) [5] techniques are appealing, exhibiting promising system performance. As for the SCC scheme, the communication and sensing (C&S) devices operate independently of each other in the same frequency band, hence resulting in interfering C&S signals. By contrast, for the ISAC scheme, the C&S devices operate by cooperating or sharing a physical site in support of the C&S functions [6].

With the global introduction of the fifth-generation (5G) new radio (NR), reliability, delay, and user experience have reached unprecedented levels. Recently, looking forward to the future multi-functional network application scenarios of smart cities, smart transportation, smart environments, and smart healthcare, purely relying on mobile communications for data transmission has been shown insufficient to cater for these demanding requirements [7]. These emerging needs have fueled the fusion of C&S paving the way for the completing concept of ISAC [8]. Indeed, heterogeneous wireless applications are omni-present and the IoT has been widely used in various domains, which jointly pave the way for the implementation of ISAC [9]. For instance, the authors of [10] proposed an ISAC system, which is capable of reducing the delay of information sharing among vehicles and of improving the date rate, while guaranteeing the safety of autonomous driving. Furthermore, in [11], an ISAC system of unmanned aerial vehicle (UAV) based on beam sharing was studied, in which UAVs could accomplish the functions of C&S. The above mentioned papers have shown that ISAC has the potential of further improving the sensing function of wireless communication networks to new levels.

In practice, the success of ISAC requires the implementation of massive end-to-end data transmission. However, it is challenging to realize information transmission with limited spectral resources. To address this issue, non-orthogonal downlink transmission (NO-DLT) is capable of delivering significant improvements in delay, energy efficiency, and throughput in contrast to the conventional orthogonal downlink transmission (O-DLT). Specifically, O-DLT can only serve a single user by exploiting the time/frequency/code domain orthogonally, while NO-DLT can simultaneously provide a balanced service for multiple devices while guaranteeing the required quality-of-service (QoS) of the devices [12]–[14]. The principle of NO-DLT is to allow controlled multiple access interference, while relying on successive interference cancellation (SIC) to decode the desired signals at the receiver [15]. For instance, in [16], a traffic offloading scheme of a device-to-device (D2D) network was investigated by using NO-DLT and the resources were optimized for ensuring that the system

M. Liu, M. Yang, and Z. Zhang are with the National Laboratory of Radar Signal Processing, Xidian University, Xi'an, Shaanxi 710071, China (e-mail: liumeng2021@163.com; mlyang@xidian.edu.cn; zmzhang_sx@163.com).

H. Li is with State Key Laboratory of Integrated Services Networks, Xidian University, Xi'an, Shaanxi 710071, China (e-mail:huifanglixd@gmail.com)

K. Zeng and G. Wang are with Huawei Technologies Co., Ltd, Chengdu, Sichuan 611731 China (e-mail: kun.zeng@huawei.com; wangguangjian@huawei.com)

A. Nallanathan is with the School of Electronic Engineering and Computer Science, Queen Mary University of London, London E1 4NS, U.K. (e-mail: a.nallanathan@qmul.ac.uk).

L. Hanzo is with the School of Electronics and Computer Science, University of Southampton, Southampton SO17 1BJ, U.K. (e-mail:lh@ecs.soton.ac.uk).

capacity was maximized. Furthermore, the multi-constraint optimization algorithm was proposed in [17] for maximizing the throughput in wireless-cached NO-DLT UAV systems. The aforementioned contributions demonstrate that NO-DLT yields significant performance gains over O-DLT in various communication scenarios, serving as a promising candidate in support of future mobile communication systems.

In order to further enhance the system's robustness and to extend the coverage area, cooperative relaying has been introduced into NO-DLT systems in [18]. For example, the authors employed a large intelligent reflecting surface as a relay to assist the end-to-end transmission of the NO-DLT system in [19], while the pairwise error probability expressions of the users were derived for quantifying the system performance attained. Furthermore, in [20], the outage probabilities (OPs) and the ergodic sum rate (ESR) of users were analyzed both in cooperative and non-cooperative NO-DLT scenarios, which demonstrated that cooperative NO-DLT is indeed capable of enhancing the overall system performance. In addition, a novel cooperative NO-DLT system was explored in [21], where the near user acted as a relay in support of a far user to communicate with the source and the closed-form expressions of the associated power allocation (PA) were obtained to maximize the sum rate at a low computational complexity.

In contrast to the half-duplex (HD) relaying schemes adopted in [18]–[21], which requires two orthogonal time slots for two-way signal transmission, full-duplex (FD) relaying requires only a single time slot to accomplish this task that potentially doubles the system's spectral efficiency. Nevertheless, the inherent loop self-interference (LSI) is unavoidable in FD systems. To address this issue, the authors of [22] adopted the natural isolation, the time-domain elimination, and the spatial suppression techniques for substantially reducing the LSI, hence facilitating the practical implementation of FD systems. Furthermore, the authors of [23] studied a FD NO-DLT vehicle-to-everything system and demonstrated that FD systems are capable of improving the latency, despite the negative impacts of LSI. Moreover, in a FD NO-DLT system supporting multiple downlink and uplink users [24], the authors further confirmed that the FD mode succeeds in improving the system's throughput and enable a fairer resource allocation than the conventional HD mode.

B. Motivation and Contribution

The authors of [6], [10], [11], [19]–[24] have respectively laid the theoretical foundations of C&S and of cooperative relaying systems. In this context, there are serval attempts in the literature for investigating ISAC and SCC systems. To elaborate the authors of [25], assumed that a radar can simultaneously perform target tracking and cooperative communication . In particular, the bounds of radar and communication as well as the optimal Fisher information were discussed to evaluate the system performance attained. Furthermore, the performance bounds of ISAC system's were developed in [26]. However, the detailed features of relay were not provided in [25] and [26]. As a further advance, single-carrier and multi-carrier SCC systems were devised in [27] and [28], respectively, and sophisticated PA schemes were proposed for maximizing the communication sum rate or receive signal-to-interference-plus-noise ratio (SINR) of radar. However, [25]–[28] were based on the conventional O-DLT philosophy without determining their optimal spectrum sharing.

As a remedy, the authors of [29] conceived a cognitive OFDM-NO-DLT ISAC system, in which the cognitive source was capable of sensing the state of the primary user for opportunistically accessing the primary network's frequency band . In particular, a PA algorithm was designed for maximizing the system capacity under the premise of a specific maximum tolerable interference caused by the cognitive source. In the cognitive Industrial IoT system of [30], multiple sensing stations worked together and transmitted the sensing information to the data center by relying on non-orthogonal communication for improving the data transmission efficiency. Another NO-DLT ISAC framework was proposed in [31], in which the transmit and receive beamformers were designed for minimizing the computational error and maximizing weighted the sum rate. Indeed, [29]–[31] provided embryonic recipes for the development of NO-DLT ISAC systems, but no cooperative ISAC schemes were considered. From a practical point of view, the integration of ISAC and NO-DLT arrangements are capable of improving the spectrum efficiency, enhance the communication reliability, and ensure resource allocation fairness. As for the cooperative ISAC systems of [25], [26], [32], and [33], the introduction of FD NO-DLT is capable of reducing the time duration of communication, thus reserving more time for sensing and further improving the exploitation of the limited resources [34]–[36]. Therefore, the performance analysis and PA schemes of FD NO-DLT ISAC networks is of pivotal significance. Against the above background, we consider a FD NO-DLT ISAC system, where a micro base station (MiBS) is capable of simultaneously realizing the functions of cooperative relaying and target sensing . A bold and definitive comparison of our contributions to the prior art is presented in Table I. Concretely, the contributions of this paper are summarized as follows:

- For the proposed FD NO-DLT ISAC system, both the exact and asymptotic lower bound expressions of the OP of IoT devices are derived along with the diversity orders attained in the high signal-to-noise ratio (SNR) regime. Furthermore, the ESR of the system considered is also investigated. To shed light on the results obtained, we further approximate the expression of the ESR. The results indicate that on the basis of realizing the extra sensing function, the ESR of the proposed FD NO-DLT ISAC system is better than that of the traditional non-cooperative NO-DLT system, despite requiring no additional power.
- The probability of successful detection (PoD) and probability of false alarm (PoFA) of the MiBS are derived for characterizing the sensing performance of the FD NO-DLT ISAC system. Also, the distance between the MiBS and the target and the radial velocity of the target are analyzed. The results obtained show that the proposed NO-DLT ISAC system outperforms its O-DLT counter-

TABLE I: Boldly and explicitly contrasting on contribution to the start-of-the-art

Paper	[4], [27], [28]	[6]	[25], [26], [32]	[29], [30]	[31]	[33]	[34]	[35]	Proposed
SCC	✓	✓							
ISAC		✓	✓	✓	✓	✓	✓	✓	✓
NO-DLT				✓	✓			✓	✓
FD							✓		✓
Cooperative			✓			✓			✓
Beamforming		✓			✓			✓	
PA	✓			✓					✓
PoD						✓	✓		✓
OP									✓
ESR									✓

part and the sensing capability is mainly determined by the transmit power of the macro base station (MaBS).

- To further improve the performance of the system considered, we formulate a pair of PA problems: *i)* A sensing-centric design (SCD), for maximizing the receive SINR of the sensing signal at the MiBS, while the IoT devices satisfy the minimum required SINR constraint; *ii)* A communication-centric design (CCD), for maximizing the sum rate of the IoT devices, while the MiBS meets the minimum SINR requirement. Finally, we analytically derive the closed-form expressions of the PA coefficients.

C. Organization and Notations

The remainder of this paper is organized as follows. Section II discusses the system model of the FD NO-DLT ISAC system. In Section III, the performance of the system considered is evaluated by deriving the exact and asymptotic OPs and the corresponding diversity orders. The ESR of the IoT devices is derived in Section IV, whileSection V analyzes the sensing performance of the system. Two PA problems are formulated in Section VI. Finally, the numerical results are provided to demonstrate the correctness of our theoretical analysis in Section VII, before concluding in Section VIII.

Notation: $\mathbb{E}[\cdot]$ represents the expectation operation, $\mathcal{CN}\left(\mu,\sigma^2\right)$ denotes a complex-valued Gaussian random variable with mean μ and variance σ^2, $\triangleq$ denotes the definition operation, $\mathrm{Ei}(\cdot)$ is the exponential integral function, $\mathbb{C}$ represents the set of complex numbers, $f_X(\cdot)$ and $F_X(\cdot)$ are the probability density function (PDF) and cumulative distribution function (CDF) of the random variable X, respectively.

II. System Model

We consider the cooperative FD NO-DLT ISAC network of Fig. 1(a), where a MaBS, S, is in charge of communication with two IoT devices[1], while a MiBS, R, is responsible for sensing the surrounding targets and for facilitating cooperative communication between the MaBS and the IoT devices located at different distances from the MaBS, namely the far IoT device D_f and the near IoT device D_n. Specifically, in order to improve the communication performance of the system, the MiBS can also act as a FD decode-and-forward (DF) relay to assist the end-to-end communication while sensing a target T[2]. In order to reduce both the power consumption and the hardware resources, we assume furthermore that the MiBS is equipped with two antennas, one for transmitting and the other for receiving signals, respectively. The MaBS and IoT devices are single-antenna devices. For the convenience of the presentation, the channel coefficients of the links $S\to R$, $S\to D_f$, $S\to D_n$, $R\to T$, $T\to R$, $R\to D_f$, and $R\to D_n$ of Fig. 1 are denoted by $h_i\in\mathbb{C}$, $i\in\{SR,SD_f,SD_n,RT,TR,RD_f,RD_n\}$, respectively. We also assumed that all the links are subject to Rayleigh fading, i.e. the channel gains $\rho_i=|h_i|^2$ all obey an exponential distribution, capturing both the path-loss and small-scale fading.[3] Next, we will discuss the signal transmission process of the FD NO-DLT ISAC system.

As for the direct links, during the t-th time slot, S intends to send the signal $y_c=\sqrt{a_nP_{\mathrm{com}}}x_n(t)+\sqrt{a_fP_{\mathrm{com}}}x_f(t)$ to D_f and D_n concurrently, where P_{com} denotes the total transmit power of S, $x_f\in\mathbb{C}$ and $x_n\in\mathbb{C}$ are the desired signals of D_f and D_n, respectively, with $\mathbb{E}\left[|x_f|^2\right]=\mathbb{E}\left[|x_n|^2\right]=1$, a_f and a_n represent the PA coefficients of S, so that $a_n+a_f=1$ and $a_f>a_n$ [39], [40]. Thus, the signals received at D_f and D_n can be expressed as

$$y_{i_1}=h_{i_1}\left(\sqrt{a_nP_{\mathrm{com}}}x_n(t)+\sqrt{a_fP_{\mathrm{com}}}x_f(t)\right)+n_{i_1},\quad(1)$$

where $i_1\in\{SD_f,SD_n\}$, $n_{i_1}\sim\mathcal{CN}(0,N_0)$ is the additive white Gaussian noise (AWGN) and N_0 is the noise power.

As for the cooperative links, the MiBS transmits $y_r=\sqrt{P_{\mathrm{sen}}}x_r(t-\tau_r)$ for sensing the target, then it receives the signals from S and the target echo, where P_{sen} is the power budget of R, $x_r\in\mathbb{C}$ denotes the transmit signal of the MiBS with $\mathbb{E}\left[|x_r|^2\right]=1$, and τ_r is the sensing signal duration. Fig. 1(b) shows the transmit and receive power at the MiBS during the t-th time slot. The signals received at the MiBS can be divided into five parts: 1) The communication signal

[1]Although only two IoT devices are considered in this paper, the network can be readily extended to multiple IoT devices. A feasible method is to reaggregate the IoT devices into different clusters, where the devices use NO-DLT within each cluster, while the O-DLT philosophy is adopted by the different clusters [37].

[2]We should point out that the essence of the multi-target system is based on the aggregate of multiple single-target echo signal, which will be set aside for our future work.

[3]Explicitly, the PDF and CDF of ρ_i are, respectively, given by $f_{\rho_i}(x)=\exp(-x/\beta_i)/\beta_i$ and $F_{\rho_i}(x)=1-\exp(-x/\beta_i)$, where $\beta_i=h/\sqrt{1+d_i^{\alpha}}$ denotes the channel's variance, $h\sim\mathcal{CN}(0,\Omega)$ is the complex channel coefficient, α denotes the path loss exponent, and d_i is the distance between the nodes [38].

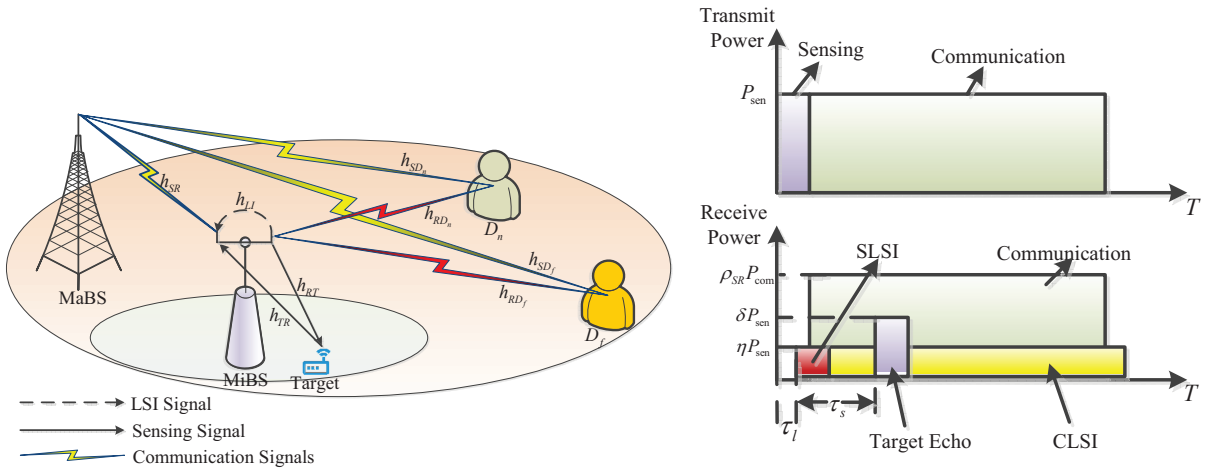

(a): An illustration of cooperative FD NO-DLT ISAC network.

(b): A diagram of the transmit and receive power at the MiBS.

Fig. 1: The cooperative FD NO-DLT ISAC system model.

transmitted form the MaBS; 2) The target echo reflected by the target; 3) The communication LSI (CLSI) transmitting the communication signal; 4) The sensing LSI (SLSI) transmitting the sensing signal; and 5) The AWGN. Therefore, the signal received at R can be expressed as[4]

$$y_{SR} = h_{SR}y_c + h_{RR}\sqrt{\delta P_{\text{sen}}}x_r\left(t-\tau_l-\tau_s\right) + h_{LI}\sqrt{\eta P_{\text{sen}}}\left[x_{LI}^c\left(t-\tau_l\right)+x_{LI}^r\left(t-\tau_l\right)\right]+n_{SR}, \quad (2)$$

where $n_{SR}\sim\mathcal{CN}\left(0,N_0\right)$ is the AWGN at R, $x_{LI}^c\in\mathbb{C}$ and $x_{LI}^r\in\mathbb{C}$ represent the CLSI and SLSI at R by transmitting the C&S signals associated with $\mathbb{E}\left[\left|x_{LI}^c\right|^2\right]=\mathbb{E}\left[\left|x_{LI}^r\right|^2\right]=1$, respectively. Furthermore, $h_{LI}\in\mathbb{C}$ is the coefficient of the LSI channel at R and $\eta\in[0,1]$ denotes the LSI cancellation capability. Specifically, $\eta=0$ indicates that the LSI is perfectly cancelled, while $\eta=1$ represents that no interference cancellation is employed between the transmit and receive antennas. Furthermore, τ_l and τ_s represent the time delay of the LSI and the target echo, respectively. Additionally, $h_{RR}\in\mathbb{C}$ is the new channel coefficient which captures the joint impact of $h_{RT}\in\mathbb{C}$ and $h_{TR}\in\mathbb{C}$ as well as $\delta\in[0,1]$ denotes the reflection factor of the target [41]. In the sequel, we introduce the CDF and PDF of ρ_{RR}, respectively.

Lemma 1. *Upon assuming that the target is moving slowly, the channel environment experienced by the signals of $R\to T$ and $T\to R$ remains approximately time-invariant, i.e., $\rho_{RT}=\rho_{TR}$. Then the CDF and PDF of ρ_{RR} are expressed as*

$$F_{\rho_{RR}}\left(x\right)=1-e^{-\frac{\sqrt{x}}{\beta_{RR}}}, \quad (3)$$

$$f_{\rho_{RR}}\left(x\right)=\frac{1}{2\beta_{RR}\sqrt{x}}e^{-\frac{\sqrt{x}}{\beta_{RR}}}. \quad (4)$$

[4]The secondary reflection from the target received by the MiBS due to the illumination of the MaBS is ignored in the data transmission, because the direct-path communication interference arriving from the MaBS is more serious than the secondary reflection [28].

Proof: By using the CDF of ρ_i, we have

$$\begin{aligned}F_{\rho_{RR}}\left(x\right)&=\Pr\left(\rho_{RR}=\rho_{RT}\rho_{TR}\leqslant x\right)\\&=\int_0^{\sqrt{x}}f_{\rho_{RT}}\left(t\right)dt=\int_0^{\sqrt{x}}f_{\rho_{TR}}\left(t\right)dt\\&=1-e^{-\frac{\sqrt{x}}{\beta_{RT}}}=1-e^{-\frac{\sqrt{x}}{\beta_{TR}}}.\end{aligned} \quad (5)$$

Using the basic variable substitution, (3) can be obtained. Then, taking the derivative of $F_{\rho_{RR}}\left(x\right)$ with respect to x, (4) can be obtained. ■

After receiving the signals, the MiBS, serving as a FD DF relay for communication, decodes and forwards the receive signals to D_f and D_n. The signals received by the IoT devices can be expressed as[5]

$$y_{i_2}=h_{i_2}\left(\sqrt{b_nP_{\text{sen}}}x_n\left(t-\tau_c\right)+\sqrt{b_fP_{\text{sen}}}x_f\left(t-\tau_c\right)\right)+n_{i_2}, \quad (6)$$

where $i_2\in\{RD_f,RD_n\}$, b_f and b_n denote the PA coefficients of the MiBS associated with $b_f+b_n=1$ and $b_f>b_n$[6] [39], $n_{i_2}\sim\mathcal{CN}\left(0,N_0\right)$ denotes the AWGN.

The receive SINRs of the communication signals can be divided into direct and cooperative links as well.

A. Direct Links

As for the direct links, the MaBS communicates with the IoT devices directly. According to the NO-DLT protocol, x_f is first decoded at D_n, and then x_n is decoded by the application

[5]It should be emphasized that if R can decode the communication signals successfully, then it will forward them to the IoT devices. Otherwise R remains silent and the cooperative links will be in a state of outage.

[6]As stated in [37], [39], [42]–[44], we assume that the IoT devices which are far/near from the MaBS, are far/near from the MiBS as well. In practice, an easily overlooked scenario exists, where the IoT devices are far/near from the MaBS, while near/far from the MiBS. In this case, the PA coefficients of the MiBS satisfy $b_f<b_n$ and $b_f+b_n=1$. The expressions of the SINRs, OP, and ESR also have to be changed according to the NO-DLT protocol.

of SIC. Thus, the SINRs of D_n associated with decoding x_f and x_n are respectively expressed as

$$\gamma_{SD_n}^{D_f} = \frac{a_f \rho_{SD_n} \gamma_c}{a_n \rho_{SD_n} \gamma_c + 1}, \tag{7}$$

$$\gamma_{SD_n}^{D_n} = a_n \rho_{SD_n} \gamma_c, \tag{8}$$

where we have $\gamma_c = P_{\rm com}/N_0$.

The receive SINR of D_f decoding its own signal over the direct link can be expressed as

$$\gamma_{SD_f}^{D_f} = \frac{a_f \rho_{SD_f} \gamma_c}{a_n \rho_{SD_f} \gamma_c + 1}. \tag{9}$$

B. Cooperative Links

As for the cooperative links, R decodes the IoT devices' desired signals in turn by employing SIC and treats the echo, CLSI, and SLSI as interferences imposed on the communication signals. Thus, the receive SINRs of x_f and x_n at R can be respectively expressed as

$$\gamma_{SR}^{D_f} = \frac{a_f \rho_{SR} \gamma_c}{a_n \rho_{SR} \gamma_c + \rho_{RR} \delta \gamma_r + 2\eta \rho_{LI} \gamma_r + 1}, \tag{10}$$

$$\gamma_{SR}^{D_n} = \frac{a_n \rho_{SR} \gamma_c}{\rho_{RR} \delta \gamma_r + 2\eta \rho_{LI} \gamma_r + 1}, \tag{11}$$

where we have $\gamma_r = P_{\rm sen}/N_0$.

If x_f is decoded successfully at R, i.e., the receive SINR of x_f exceeds the outage threshold, x_f will be sent to D_f. Then, the receive SINR of x_f at D_f can be expressed as

$$\gamma_{RD_f}^{D_f} = \frac{b_f \rho_{RD_f} \gamma_r}{b_n \rho_{RD_f} \gamma_r + 1}. \tag{12}$$

Similarly, if both x_f and x_n are decoded successfully at R, the signals will be sent to the D_n. At D_n, the high-power signal x_f will be decoded first and then it will be remodulated and subtracted from D_n to cancel its effect until x_n is detected. Therefore, the receive SINRs of x_f and x_n at D_n are respectively expressed as

$$\gamma_{RD_n}^{D_f} = \frac{b_f \rho_{RD_n} \gamma_r}{b_n \rho_{RD_n} \gamma_r + 1}, \tag{13}$$

$$\gamma_{RD_n}^{D_n} = b_n \rho_{RD_n} \gamma_r. \tag{14}$$

In the following, the communication performance of the system considered is evaluated by investigating both the exact and asymptotic OPs, diversity orders, and the ESR of the IoT devices. As a further development, the PoFA and PoD of the MiBS are respectively derived for characterizing the sensing performance. For the sake of convenience, the significant performance analysis identifiers are summarized in Table II.

III. OP Analysis

The OP is an important performance metric of a system, which is related to the average SINRs of the links and the channel fading parameters. Therefore, in this section, we derive the exact OP lower bound of the IoT devices. In order to glean deeper insights concerning the OP, both the asymptotic OPs as well as the diversity orders are analyzed for further characterizing the performance of the proposed FD NO-DLT ISAC system.

TABLE II: Summary of the notations

Identifier	Description	Identifier	Description
$\mathrm{P}_{\rm out}^{D_f}$	OP of D_f	$\mathrm{P}_{\rm out}^{D_n}$	OP of D_n
$\mathrm{P}_{\rm out}^{D_f,\infty}$	Asy. OP of D_f	$\mathrm{P}_{\rm out}^{D_n,\infty}$	Asy. OP of D_n
D_O^f	Diversity order of D_f	D_O^n	Diversity order of D_n
$R_{\rm ave}^f$	ER of D_f	$R_{\rm ave}^n$	ER of D_n
$R_{\rm ave}^{ap,f}$	Asy. ER of D_f	$R_{\rm ave}^{ap,n}$	Asy. ER of D_f
$R_{\rm ave}^{\rm sum}$	ESR	$R_{\rm ave}^{ap,\rm sum}$	Asy. ESR
$\mathrm{P}_{\rm fa}$	PoFA	$\mathrm{P}_{\rm d}$	PoD

A. Exact OP

An outage event is encountered at D_f, when one of the following two events occurs. Case *i)* Neither R nor D_f can successfully decode x_f from the $S \to R$ and $S \to D_f$ links; Case *ii)* R decodes and forwards x_f to D_f, while D_f fails to decode the desired signal from the $R \to D_f$ and $S \to D_f$ links. Thus, the OP of D_f is expressed as[7]

$$\mathrm{P}_{\rm out}^{D_f} = \underbrace{\Pr\left(\max\left(\gamma_{SR}^{D_f}, \gamma_{SD_f}^{D_f}\right) < \gamma_{\mathrm{th}_f}\right)}_{I_1} + \underbrace{\Pr\left(\gamma_{SR}^{D_f} \geqslant \gamma_{\mathrm{th}_f}, \max\left(\gamma_{RD_f}^{D_f}, \gamma_{SD_f}^{D_f}\right) < \gamma_{\mathrm{th}_f}\right)}_{I_2}, \tag{15}$$

where γ_{th_f} denotes the SNR threshold of x_f, while I_1 refers to Case *i* and I_2 refers to Case *ii*. The exact OP expression of D_f for the FD NO-DLT ISAC system considered is given in the following theorem.

Theorem 1. *The exact OP of D_f device is expressed as*

$$\mathrm{P}_{\rm out}^{D_f} = \left(1 - e^{-\frac{\theta_1}{\beta_{SD_f}}}\right)\left\{1 - \frac{\beta_{SR}}{2\beta_{RR}\left(\beta_{SR} + 2\eta\beta_{LI}\gamma_r\theta_1\right)}\sqrt{\frac{\pi\beta_{SR}}{\delta\gamma_r\theta_1}} \times e^{\frac{\beta_{SR}}{4\beta_{RR}^2\delta\gamma_r\theta_1} - \frac{\theta_1}{\beta_{SR}} - \frac{\varphi_1}{\beta_{RD_f}}}\left[1 - \mathrm{erfc}\left(\frac{1}{2\beta_{RR}}\sqrt{\frac{\beta_{SR}}{\delta\gamma_r\theta_1}}\right)\right]\right\}, \tag{16}$$

where $\theta_1 = \gamma_{\mathrm{th}_f}/\left(a_f\gamma_c - a_n\gamma_c\gamma_{\mathrm{th}_f}\right)$ with $a_f > a_n\gamma_{\mathrm{th}_f}$, $\varphi_1 = \gamma_{\mathrm{th}_f}/\left(b_f\gamma_r - b_n\gamma_r\gamma_{\mathrm{th}_f}\right)$ with $b_f > b_n\gamma_{\mathrm{th}_f}$, otherwise $\mathrm{P}_{\rm out}^{D_f} = 1$ and $\mathrm{erfc}\left(\cdot\right)$ denotes the complementary error function which is expressed as

$$\mathrm{erfc}\left(z\right) = \frac{2}{\sqrt{\pi}}\int_z^\infty e^{-t^2}dt. \tag{17}$$

Proof: See Appendix A. ■

Similarly, an outage event occurs at D_n when: Case *iii)* Either x_f or x_n cannot be decoded successfully from the $S \to D_n$ and $S \to R$ links; Case *iv)* R decodes and forwards x_f and x_n to D_n, while D_n fails to decode either of them from the $S \to D_n$ and $R \to D_n$ links. Thus, the OP of D_n is expressed as (18), shown at the top of the next page, where γ_{th_n} denotes the SNR threshold of x_n, I_3 refers to Case *iii)* and I_4 refers to Case *iv)*. The exact OP expression of D_n

[7]The selection combining (SC) scheme is adopted to calculate the OPs of the IoT devices, since it has low implementation cost and does not reduce the diversity gain. Our analysis may also be reality extended to the maximal ratio combining (MRC) scheme, which will be set aside for our future work.

$$\mathrm{P}_{\mathrm{out}}^{D_n} = \underbrace{\Pr\left(\min\left(\frac{\gamma_{SR}^{D_f}}{\gamma_{\mathrm{th}_f}}, \frac{\gamma_{SR}^{D_n}}{\gamma_{\mathrm{th}_n}}\right) < 1, \min\left(\frac{\gamma_{SD_n}^{D_f}}{\gamma_{\mathrm{th}_f}}, \frac{\gamma_{SD_n}^{D_n}}{\gamma_{\mathrm{th}_n}}\right) < 1\right)}_{I_3}$$
$$+ \underbrace{\Pr\left(\min\left(\frac{\gamma_{SR}^{D_f}}{\gamma_{\mathrm{th}_f}}, \frac{\gamma_{SR}^{D_n}}{\gamma_{\mathrm{th}_n}}\right) \geqslant 1, \min\left(\frac{\gamma_{RD_n}^{D_f}}{\gamma_{\mathrm{th}_f}}, \frac{\gamma_{RD_n}^{D_n}}{\gamma_{\mathrm{th}_n}}\right) < 1, \min\left(\frac{\gamma_{SD_n}^{D_f}}{\gamma_{\mathrm{th}_f}}, \frac{\gamma_{SD_n}^{D_n}}{\gamma_{\mathrm{th}_n}}\right) < 1\right)}_{I_4}. \quad (18)$$

for the FD NO-DLT ISAC considered system is given in the following theorem.

Theorem 2. *The exact OP of D_n device is expressed as*

$$\mathrm{P}_{\mathrm{out}}^{D_n} = \left(1 - e^{-\frac{\theta}{\beta_{SD_n}}}\right)\left\{1 - \frac{\beta_{SR}}{2\beta_{RR}\left(\beta_{SR} + 2\eta\beta_{LI}\gamma_r\theta\right)}\sqrt{\frac{\pi\beta_{SR}}{\delta\gamma_r\theta}} \times e^{\frac{\beta_{SR}}{4\beta_{RR}^2\delta\gamma_r\theta} - \frac{\theta}{\beta_{SR}} - \frac{\varphi}{\beta_{RD_n}}}\left[1 - \mathrm{erfc}\left(\frac{1}{2\beta_{RR}}\sqrt{\frac{\beta_{SR}}{\delta\gamma_r\theta}}\right)\right]\right\}, \quad (19)$$

where $\theta \triangleq \max(\theta_1, \theta_2)$, $\theta_2 = \gamma_{\mathrm{th}_n}/(a_n\gamma_c)$, $\varphi \triangleq \max(\varphi_1, \varphi_2)$, $\varphi_2 = \gamma_{\mathrm{th}_n}/(b_n\gamma_r)$.

Proof: Similar to Appendix A, substituting (7), (8), and (10)-(14) into (18), and then using the PDFs and CDFs of ρ_i, (19) can be obtained through a series of mathematical manipulations. ∎

Remark 1. *We can observe from Theorem 1 and Theorem 2 that the OP of D_f depends on the decoding capability of x_f at R and D_f, while the OP of D_n is related to the decoding capability of both x_f and x_n at R and D_f. More particularly, when considering the direct links, the OPs of the far and near IoT devices are limited by the channel fading, which are respectively given by $\mathrm{P}_{\mathrm{out}}^{D_f} = 1 - \exp\left(-\theta_1/\beta_{SD_f}\right)$ and $\mathrm{P}_{\mathrm{out}}^{D_n} = 1 - \exp\left(-\theta/\beta_{SD_n}\right)$. When considering the cooperative links, the CLSI, SLSI, and echo have a significant impact on the OPs of the IoT devices.*

B. Diversity Order

To obtain further insights concerning on the FD NO-DLT ISAC system, the diversity orders of the IoT devices in the high-SNR regime are analyzed in this subsection. The diversity order is defined as [45]

$$D_O = -\lim_{\Upsilon\to\infty}\frac{\log\left(\mathrm{P}_{\mathrm{out}}^{\infty}\right)}{\log\Upsilon}, \quad (20)$$

where $\Upsilon \in \{\gamma_c, \gamma_r\}$ and $\mathrm{P}_{\mathrm{out}}^{\infty}$ is the asymptotic OP of the IoT devices in the high-SNR regime.

The asymptotic OPs of D_f and D_n in the high-SNR regime are summarized in the following corollaries.

Corollary 1. *The asymptotic OP of D_f is expressed as*

$$\mathrm{P}_{\mathrm{out}}^{D_f,\infty} \approx \frac{\theta_1}{\beta_{SD_f}}\left\{1 - \left(1 - \frac{\varphi_1}{\beta_{RD_f}}\right)\frac{\beta_{SR}}{2\beta_{RR}\left(\beta_{SR} + 2\eta\beta_{LI}\theta_1^*\right)} \times \sqrt{\frac{\pi\beta_{SR}}{\delta\theta_1^*}}e^{\frac{\beta_{SR}}{4\beta_{RR}^2\delta\theta_1^*}}\left[1 - \mathrm{erfc}\left(\frac{1}{2\beta_{RR}}\sqrt{\frac{\beta_{SR}}{\delta\theta_1^*}}\right)\right]\right\}, \quad (21)$$

where we have $\theta_1^* = \gamma_{\mathrm{th}_f}/\left(a_f - a_n\gamma_{\mathrm{th}_f}\right)$.

Proof: See Appendix B. ∎

By substituting (21) into (20), we can show that the diversity order of D_f in the high-SNR regime is $D_O^f = 1$.

Corollary 2. *The asymptotic OP of D_n is expressed as*

$$\mathrm{P}_{\mathrm{out}}^{D_n,\infty} \approx \frac{\theta}{\beta_{SD_n}}\left\{1 - \left(1 - \frac{\varphi}{\beta_{RD_n}}\right)\frac{\beta_{SR}}{2\beta_{RR}\left(\beta_{SR} + 2\eta\beta_{LI}\theta^*\right)} \times \sqrt{\frac{\pi\beta_{SR}}{\delta\theta^*}}e^{\frac{\beta_{SR}}{4\beta_{RR}^2\delta\theta^*}}\left[1 - \mathrm{erfc}\left(\frac{1}{2\beta_{RR}}\sqrt{\frac{\beta_{SR}}{\delta\theta^*}}\right)\right]\right\}, \quad (22)$$

where we have $\theta^* \triangleq \max(\theta_1^*, \theta_2^*)$ *and* $\theta_2^* = \gamma_{\mathrm{th}_n}/a_n$.

Proof: Similar to Appendix upon, substituting (7), (8) and (10)-(14) into (18), with the PDF and CDF of ρ_i, (22) can be obtained after some mathematical manipulations. ∎

By substituting (22) into (20), the diversity order of D_n in the high-SNR regime is $D_O^n = 1$.

Remark 2. *We can observe from (21) and (22), that the OPs of cooperative links are constant in the high-SNR regime due to the existence of the CLSI, SLSI and echo, which further leads to having a zero diversity order for the cooperative links. In this case, the diversity orders of the IoT devices are provided by those of the direct links. Specifically, for the direct links, the asymptotic OPs of the far and near IoT devices are respectively given by $\mathrm{P}_{\mathrm{out}}^{D_f,\infty} \approx \theta_1/\beta_{SD_f}$ and $\mathrm{P}_{\mathrm{out}}^{D_n,\infty} \approx \theta/\beta_{SD_n}$, while the corresponding diversity orders are $D_O^f = D_O^n = 1$.*

IV. ESR Analysis

The ESR represents the sum rate of the IoT devices per unit time, which characterize the fading performance of the system from a different perspective than the OP. Thus, in this section, the ESR of the IoT devices is explored for the FD NO-DLT ISAC system considered.

The achievable rates of x_f and x_n are respectively expressed as [39]

$$R_f = \underbrace{\log_2\left(1+\min\left(\gamma_{SR}^{D_f},\gamma_{RD_f}^{D_f},\gamma_{RD_n}^{D_f}\right)\right)}_{R_f^1} + \underbrace{\log_2\left(1+\min\left(\gamma_{SD_f}^{D_f},\gamma_{SD_n}^{D_f}\right)\right)}_{R_f^2}, \quad (23)$$

$$R_n = \underbrace{\log_2\left(1+\min\left(\gamma_{SR}^{D_n},\gamma_{RD_n}^{D_n}\right)\right)}_{R_n^1} + \underbrace{\log_2\left(1+\gamma_{SD_n}^{D_n}\right)}_{R_n^2}. \quad (24)$$

Then, the ergodic rates (ERs) of D_f and D_n are respectively given by

$$R_{\text{ave}}^f = R_{\text{ave}}^{f,1} + R_{\text{ave}}^{f,2} = \mathbb{E}\left[R_f^1\right] + \mathbb{E}\left[R_f^2\right], \quad (25)$$

$$R_{\text{ave}}^n = R_{\text{ave}}^{n,1} + R_{\text{ave}}^{n,2} = \mathbb{E}\left[R_n^1\right] + \mathbb{E}\left[R_n^2\right]. \quad (26)$$

Theorem 3. *The ER of the far IoT device is expressed as (27), shown at the top of the next page, where* $g_c(w) = (a_f\gamma_c - a_n\gamma_c w)/w$ *and* $g_r(w) = (b_f\gamma_r - b_n\gamma_r w)/w$.

The ER of the near IoT device is expressed as (28), shown at the top of the next page, where $q_c(w) = a_n\gamma_c/w$ *and* $q_r(w) = b_n\gamma_r/w$.

Proof: See Appendix C. ∎

Thus, the ESR of the IoT devices is expressed as

$$R_{\text{ave}}^{\text{sum}} = R_{\text{ave}}^f + R_{\text{ave}}^n. \quad (29)$$

From (27) and (28), we can observe that it is challenging to obtain the exact ESR of the IoT devices, if not impossible. As a compromise, we analyze the ESR by adopting some approximations. The approximate ERs of D_f and D_n are given in the following corollary.

Corollary 3. *The approximated ER of the far IoT device is expressed as (30), shown at the top of the next page.*

The approximate ER of the near IoT device is formulated as (31), shown at the top of the next page.

Based on (30) and (31), the ESR of the IoT devices can be approximated as

$$R_{\text{ave}}^{ap,\text{sum}} \approx R_{\text{ave}}^{ap,f} + R_{\text{ave}}^{ap,n}. \quad (32)$$

Proof: See Appendix D. ∎

Remark 3. *From Theorem 3 and Corollary 3, we can observe that the sensing signal has a negative impact on the ESR of the IoT devices. For the cooperative links, the ERs of* D_f *and* D_n *respectively tend to be* $\log_2\left[1+a_f\beta_{SR}/\left(a_n\beta_{SR}+2\beta_{RR}^2\delta+2\eta\beta_{LI}\right)\right]$ *and* $\log_2\left[1+a_n\beta_{SR}/\left(2\beta_{RR}^2\delta+2\eta\beta_{LI}\right)\right]$ *in the high-SNR regime. For the non-cooperative scheme, the sum rate reduces to* $R_{\text{sum}} = R_f^2 + R_n^2$. *Moreover, it is noteworthy that if the MiBS operates in the HD mode, the rates of the IoT devices can be increased due to the absence of CLSI.*

V. PoD Analysis

As for sensing, the fundamental task is to find the target and make the correct identification, which is the premise of target parameter estimation. Generally, the receive echo is a mixture of the desired signal, interference, and noise. The presence/absence of the target can be determined by the power of the receive signals. Assuming that H_0 represents the null hypothesis and H_1 includes echoes, interference and AWGN, they can be defined as

$$\begin{aligned} H_0: y_{SR} &= h_{SR}y_c + h_{LI}\sqrt{\eta P_{\text{sen}}}\left(x_{LI}^c + x_{LI}^r\right) + n_{SR}, \\ H_1: y_{SR} &= h_{SR}y_c + h_{RR}\sqrt{\delta}y_r + h_{LI}\sqrt{\eta P_{\text{sen}}}\left(x_{LI}^c + x_{LI}^r\right) + n_{SR}, \end{aligned} \quad (33)$$

where y_c and y_r denote the signals transmitted by the MaBS and the MiBS, respectively. Indeed, PoFA and PoD are adopted for characterizing the sensing performance. Specifically, if the receive power of the MiBS exceeds the preset threshold under H_0, the MiBS concludes that a target is present and hence makes the wrong inference. By contrast, the target can be sensed successfully. Hence, it can be inferred from (33) that the receive power of the MiBS is a non-central Chi-square distributed random variable having a degree-of-freedom (DoF) of four under H_0 and five under H_1 [46]. Therefore, according to H_0, the false-alarm probability of the MiBS is expressed as [47]

$$\text{P}_{\text{fa}} = Q_2\left(\sqrt{\frac{2\left(\rho_{SR}P_{\text{com}} + 2\eta\rho_{LI}P_{\text{sen}}\right)}{N_0}}, \sqrt{\frac{2\zeta}{N_0}}\right), \quad (34)$$

where ζ denotes the sensing threshold and $Q(\cdot,\cdot)$ represents the Marcum Q-function [48]. The PoD of the MiBS according to H_1 can be expressed as [33]

$$\text{P}_{\text{d}} = Q_{\frac{5}{2}}\left(\sqrt{\frac{2\left(\rho_{SR}P_{\text{com}} + \eta\rho_{LI}P_{\text{sen}} + \rho_{RR}\delta P_{\text{sen}}\right)}{N_0}}, \sqrt{\frac{2\zeta}{N_0}}\right). \quad (35)$$

In the following, we adopt the receive signal of the MiBS for inferring the presence/absence of the target. According to (2), the power received at the MiBS can be expressed as

$$\mathbb{E}\left[|y_{SR}|^2\right] = \rho_{SR}P_{\text{com}} + \rho_{RR}\delta P_{\text{sen}} + 2\eta\rho_{LI}P_{\text{sen}} + N_0. \quad (36)$$

Naturally, $\mathbb{E}\left[|y_{SR}|^2\right]$, ρ_{SR}, P_{com}, P_{sen}, and N_0 are known for the MiBS. Then the information related to the target can be expressed as

$$\rho_{RR}\delta = \frac{\mathbb{E}\left[|y_{SR}|^2\right] - 2\eta\rho_{LI}P_{\text{sen}} - \rho_{SR}P_{\text{com}} - N_0}{P_{\text{sen}}}. \quad (37)$$

Apart from the target detection, the measurements of target parameters are also significant. In this context, the distance between the target and the MiBS as well as the velocity of the target are analyzed according to the echo at the receiver.

According to the time difference between transmitting the sensing signal and receiving the target echo, the distance between the MiBS and target may be expressed as [49]

$$d_{RT} = \frac{c}{2}\left(\tau_l + \tau_s\right), \quad (38)$$

$$R_{\text{ave}}^{f}=\int_{0}^{\infty}\frac{g_{c}^{\frac{3}{2}}\left(w_{1}\right)e^{\frac{\beta_{SR}g_{c}(w_{1})}{4\beta_{RR}^{2}\delta\gamma_{r}}-\frac{1}{\beta_{SR}g_{c}(w_{1})}-\frac{1}{\beta_{RD_{f}}g_{r}(w_{1})}-\frac{1}{\beta_{RD_{n}}g_{r}(w_{1})}}\left[1-\operatorname{erfc}\left(\frac{1}{2\beta_{RR}}\sqrt{\frac{g_{c}(w_{1})\beta_{SR}}{\delta\gamma_{r}}}\right)\right]}{\left(1+w_{1}\right)\left(\beta_{SR}g_{c}\left(w_{1}\right)+2\eta\beta_{LI}\gamma_{r}\right)}dw_{1}$$
$$\times\frac{\beta_{SR}}{2\beta_{RR}\ln 2}\sqrt{\frac{\pi\beta_{SR}}{\delta\gamma_{r}}}+\frac{1}{\ln 2}\int_{0}^{\infty}\frac{1}{1+w_{2}}e^{-\frac{1}{\beta_{SD_{f}}g_{c}(w_{2})}-\frac{1}{\beta_{SD_{n}}g_{c}(w_{2})}}dw_{2}. \tag{27}$$

$$R_{\text{ave}}^{n}=\int_{0}^{\infty}\frac{\frac{q_{c}^{\frac{3}{2}}(w_{3})}{\left(\beta_{SR}q_{c}(w_{3})+2\eta\beta_{LI}\gamma_{r}\right)}e^{\frac{\beta_{SR}g_{c}(w_{3})}{4\beta_{RR}^{2}\delta\gamma_{r}}-\frac{1}{\beta_{SR}q_{c}(w_{3})}-\frac{1}{\beta_{RD_{n}}q_{r}(w_{3})}}\left[1-\operatorname{erfc}\left(\frac{1}{2\beta_{RR}}\sqrt{\frac{q_{c}(w_{3})\beta_{SR}}{\delta\gamma_{r}}}\right)\right]}{1+w_{3}}dw_{3}$$
$$\times\frac{\beta_{SR}}{2\beta_{RR}\ln 2}\sqrt{\frac{\pi\beta_{SR}}{\delta\gamma_{r}}}-\frac{1}{\ln 2}e^{\frac{1}{\beta_{SD_{n}}a_{n}\gamma_{c}}}\operatorname{Ei}\left(-\frac{1}{\beta_{SD_{n}}a_{n}\gamma_{c}}\right). \tag{28}$$

$$R_{\text{ave}}^{ap,f}\approx\frac{1}{\ln 2}\left\{\ln\left[1+\min\left(\frac{a_{f}\beta_{SD_{f}}\gamma_{c}}{a_{n}\beta_{SD_{f}}\gamma_{c}+1},\frac{a_{f}\beta_{SD_{n}}\gamma_{c}}{a_{n}\beta_{SD_{n}}\gamma_{c}+1}\right)\right]\right.$$
$$\left.+\ln\left[1+\min\left(\frac{a_{f}\beta_{SR}\gamma_{c}}{a_{n}\beta_{SR}\gamma_{c}+2\beta_{RR}^{2}\delta\gamma_{r}+2\eta\beta_{LI}\gamma_{r}+1},\frac{b_{f}\beta_{RD_{f}}\gamma_{r}}{b_{n}\beta_{RD_{f}}\gamma_{r}+1},\frac{b_{f}\beta_{RD_{n}}\gamma_{r}}{b_{n}\beta_{RD_{n}}\gamma_{r}+1}\right)\right]\right\}. \tag{30}$$

$$R_{\text{ave}}^{ap,n}\approx\frac{1}{\ln 2}\left\{\ln\left(1+a_{n}\beta_{SD_{n}}\gamma_{c}\right)+\ln\left[1+\min\left(\frac{a_{n}\beta_{SR}\gamma_{c}}{2\beta_{RR}^{2}\delta\gamma_{r}+2\eta\beta_{LI}\gamma_{r}+1},b_{n}\beta_{RD_{n}}\gamma_{r}\right)\right]\right\}. \tag{31}$$

where c is the speed of light, and $(\tau_l+\tau_s)$ denotes the time delay of the target.

As a further step, the radial velocity of the target can be written as [49]

$$v_T=\frac{c}{2f_s}\left|f_e-f_s\right|, \tag{39}$$

where $|f_e-f_s|$ denotes Doppler frequency, while f_s and f_e respectively represent the frequency of the transmitted signal and the received echo, which can be observed from the MiBS.

Remark 4. *It can be observed from (34) that for a given PoFA, there exists a unique detection threshold corresponding to it, and then the PoD can be obtained. In addition, we reiterate that if the target is outside the range of sensing, the result obtained through (37) may be generated by the randomness of noise, thus further signal processing is essential to determine whether the target exists.*

Remark 5. *It should be noted that as the basis of target detection, it is essential to derive the PoD expression for characterizing the sensing performance of the ISAC system considered. In contrast to the mature cognitive radio networks, in the ISAC systems, the target to be detected is non-cooperative, which is challenging for the MiBS. Therefore, in the following, we design a PA scheme for maximizing the received SINR of the sensing signal, so that the PoD can be further improved.*

VI. Power Allocation Schemes

Having accurate PA is essential to enhance the system performance and the resource utilization. Therefore, in this section, a pair of PA designs are proposed for the FD NO-DLT ISAC system considered, namely, SCD and CCD. Specifically, SCD aims for maximizing the receive SINR of the sensing signal at the MiBS under the IoT devices' QoS constraints. By contrast, CCD aims for maximizing the IoT devices' sum rate under the constraints of minimum SINR requirements. It is worth stating that both SCD and CCD are of practical interest [27], [28]. According to (34) and (35), it can be observed that increasing the SINR of the sensing signal improves the receive echo power and enhances the sensing performance. This means that for SCD, increasing the receive SINR of sensing signal improves the PoD and guarantees the decoding requirements for the cooperative links. Moreover, the proportion of the sensing signal is fixed at a prescribed PoD, which indicates that for CCD, the sum rate is improved, while meeting the sensing performance target. Indeed, these PA problems are meaningful for ISAC systems in practical scenarios from a range of different perspectives. To this end, the receive SINR of x_r at the MiBS, which according to (2) can be expressed as

$$\gamma_{SR}^{R}=\frac{\delta\rho_{RR}\gamma_{r}}{\rho_{SR}\gamma_{c}+2\eta\rho_{LI}\gamma_{r}+1}. \tag{40}$$

A. SCD Scheme

On the basis of (40), the SCD scheme can be optimized as

$$\underset{P_{\rm com},P_{\rm sen},a_n,b_n}{\text{maximize}} \quad \gamma_{SR}^{R} \tag{41}$$

$$\text{s.t.} \ \min\left(\gamma_{SR}^{D_f},\gamma_{RD_f}^{D_f},\gamma_{RD_n}^{D_f}\right) \geqslant \gamma_{\text{th}_f}, \tag{41a}$$

$$\min\left(\gamma_{SR}^{D_n},\gamma_{RD_n}^{D_n}\right) \geqslant \gamma_{\text{th}_n}, \tag{41b}$$

$$0 \leqslant P_{\rm com} \leqslant P_{\max},\ 0 \leqslant P_{\rm sen} \leqslant P_{\max}, \tag{41c}$$

$$a_n + a_f = 1, 0 < a_n < a_f < 1,$$

$$b_n + b_f = 1, 0 < b_n < b_f < 1, \tag{41d}$$

where (41a) and (41b) indicate that x_f and x_n respectively can be decoded successfully from the cooperative links, (41c) characterizes the power budget of the MaBS and MiBS, and (41d) guarantees the enforceability of NO-DLT.

Substituting (10)-(12) into (41a) and (41b), the PA problem can be rewritten as

$$\underset{P_{\rm com},P_{\rm sen},a_n,b_n}{\text{maximize}} \quad \gamma_{SR}^{R} \tag{42}$$

$$\text{s.t.} \ P_{\rm com} \geqslant \left(\delta\rho_{RR} + 2\eta\rho_{LI}\right)\theta' P_{\rm sen} + N_0\theta', \tag{42a}$$

$$P_{\rm sen} \geqslant C_1, \ (41\text{c}), \ (41\text{d}), \tag{42b}$$

where $\theta' = \theta^*/\rho_{SR}$, $C_1 \triangleq \max\left(C_{11}, C_{12}, C_{13}\right)$, $C_{11} = \varphi_1^*/\rho_{RD_f}$, $C_{12} = \varphi_1^*/\rho_{RD_n}$, $C_{13} = N_0\gamma_{\text{th}_n}/b_n\rho_{RD_n}$, and $\varphi_1^* = N_0\gamma_{\text{th}_f}/\left(b_f - b_n\gamma_{\text{th}_f}\right)$, while θ_1^* and θ^* can be obtained from Corollary 1 and Corollary 2, respectively.

Observe from (42) that the PA coefficients are coupled, thus it is difficult to obtain them simultaneously. In the following, we apply the popular alternating optimization (AO) technique and the expressions of $P_{\rm sen}$, $P_{\rm com}$, a_n, and b_n are derived iteratively.

Substituting (40) into (42), we can observe that γ_{SR}^{R} is a convex function, since as $\partial^2\gamma_{SR}^{R}/\partial P_{sen}^2 < 0$. Therefore, the Lagrangian function of (42) can be expressed as

$$\begin{aligned} L_1\left(P_{\rm sen},\lambda_{11},\lambda_{12},\lambda_{13}\right) &= \frac{\delta\rho_{RR}P_{\rm sen}}{\rho_{SR}P_{\rm com} + 2\eta\rho_{LI}P_{\rm sen} + 1} \\ &+ \lambda_{11}\left[P_{\rm com} - \left(\delta\rho_{RR} + 2\eta\rho_{LI}\right)\theta' P_{\rm sen} - N_0\theta'\right] \\ &+ \lambda_{12}\left(P_{\rm sen} - C_1\right) + \lambda_{13}\left(P_{\max} - P_{\rm sen}\right), \end{aligned} \tag{43}$$

where λ_{11}, λ_{12}, and λ_{13} are the non-negative Lagrange multipliers with respect to the constraints (42a), (42b), and (41c), respectively. Examining the Karush-Kuhn-Tucker (KKT) condition for $L\left(\cdot\right)$ yields

$$\begin{aligned} \frac{\partial L_1}{\partial P_{\rm sen}} &= \frac{\delta\rho_{RR}\left(\rho_{SR}P_{\rm com} + 1\right)}{\left(\rho_{SR}P_{\rm com} + 2\eta\rho_{LI}P_{\rm sen} + 1\right)^2} \\ &- \lambda_{11}\left(\delta\rho_{RR} + 2\eta\rho_{LI}\right)\theta' + \lambda_{12} - \lambda_{13} = 0. \end{aligned} \tag{44}$$

After some mathematical manipulations, the PA coefficient $P_{\rm sen}^*$ with the fixed multipliers is expressed as (45), shown at the top of the next page, where $\left(\Delta\right)^+ \triangleq \max\left(0,\Delta\right)$.

Next, we optimize $P_{\rm com}$ at fixed $P_{\rm sen}$, a_n, and b_n, where the objective function in (42) is monotonically decreasing with respect to $P_{\rm com}$. Herewith, according to (41c), (42a), and (45), the PA coefficient $P_{\rm com}^*$ is expressed as

$$P_{\rm com}^* = \min\left[\left(\delta\rho_{RR} + 2\eta\rho_{LI}\right)\theta' P_{\rm sen} + N_0\theta', P_{\max}\right]. \tag{46}$$

The problem can be solved by employing the subgradient method, and the subgradient at $(\lambda_{11},\lambda_{12},\lambda_{13})$ is written as

$$\mathbf{d} = \left[d_{11}, d_{12}, d_{13}\right], \tag{47}$$

where $d_{11} = P_{\rm com}^* - \left(\delta\rho_{RR} + 2\eta\rho_{LI}\right)\theta' P_{\rm sen}^* - N_0\theta'$, $d_{12} = P_{\rm sen}^* - C_1$, and $d_{13} = P_{\max} - P_{\rm sen}^*$.

Finally, let us turn our attention to the PA coefficients of a_n and b_n at fixed $P_{\rm com}$ and $P_{\rm sen}$. Observe from (42) that γ_{SR}^{R} is independent of a_n and b_n, while $P_{\rm com}^*$ and $P_{\rm sen}^*$ are related to a_n and b_n upon combining with (40), (45), and (46), we can observe that γ_{SR}^{R} is decreasing with respect to θ^*. By exploiting this property, the PA problem can be reformulated to find the minimum θ^*. Observe from Corollary 1 and Corollary 2 that θ_1^* is monotonically increasing, while θ_2^* is decreasing with respect to a_n. Therefore, θ^* can be expressed as

$$\theta^* = \begin{cases} \theta_2^*, \ \text{if} \ a_n \in \left(0, a_n^\dagger\right] \\ \theta_1^*, \ \text{if} \ a_n \in \left[a_n^\dagger, 0.5\right) \end{cases}, \tag{48}$$

where $a_n^\dagger = \gamma_{\text{th}_n}/\left(\gamma_{\text{th}_f} + \gamma_{\text{th}_n} + \gamma_{\text{th}_f}\gamma_{\text{th}_n}\right)$. According to the characteristics of θ_1^* and θ_2^*, θ^* can be minimized if and only if $a_n = a_n^\dagger$.

Furthermore, we can obtain $b_n^\dagger = \rho_{RD_f}\gamma_{\text{th}_n}/\left(\rho_{RD_f}\gamma_{\text{th}_n} + \rho_{RD_n}\gamma_{\text{th}_f} + \rho_{RD_f}\gamma_{\text{th}_n}\gamma_{\text{th}_f}\right)$ by using the same method. Therefore, a_n^* and b_n^* are expressed as

$$a_n^* = \min\left(a_n^\dagger, 0.5 - \sigma\right), \tag{49}$$

$$b_n^* = \min\left(b_n^\dagger, 0.5 - \sigma\right), \tag{50}$$

where $\sigma > 0$ and $\sigma \to 0$.

The alternating optimization algorithm of the SCD scheme is summarized in Algorithm 1, which iteratively determines the PA coefficients.

Remark 6. *For the SCD scheme, the computational complexity of the algorithm is on the order of $O\left[\left(K_1+2\right)K_2\right]$, where K_1 is the number of iterations required for finding the optimal Lagrangian, K_2 is the number of iterations in the main loop.*

B. CCD Scheme

Now, we switch our focus to the CCD scheme. Based on (23) and (24), the CCD scheme can be optimized as follows:

$$\underset{P_{\rm com},P_{\rm sen},a_n,b_n}{\text{maximize}} \quad R_{\rm sum} \tag{51}$$

$$\text{s.t.} \ \min\left(\gamma_{SR}^{D_f},\gamma_{RD_f}^{D_f},\gamma_{RD_n}^{D_f},\gamma_{SD_f}^{D_f},\gamma_{SD_n}^{D_f}\right) \geqslant \gamma_{\text{th}_f}, \tag{51a}$$

$$\min\left(\gamma_{SR}^{D_n},\gamma_{RD_n}^{D_n},\gamma_{SD_n}^{D_n}\right) \geqslant \gamma_{\text{th}_n}, \tag{51b}$$

$$\gamma_{SR}^{R} \geqslant \kappa, \ (41\text{c}), \ (41\text{d}), \tag{51c}$$

where (51a) and (51b) indicate that the communication signals can be decoded successfully from the cooperative links, (51c) is the receive SINR of x_r constraint at the MiBS, κ denotes the lower bound of the receive SINR and $R_{\rm sum}$ can be further expressed as (52), shown at the top of the next page[8], where

[8]It should be noted that due to the intractability of the sum rate, it is extremely difficult to obtain the exact PA factors, thus we focus on the approximate sum rate in the high-SNR regimes as in [37] and [50].

$$P_{\text{sen}}^{*}=\left(\frac{1}{2\eta\rho_{LI}}\left[\sqrt{\frac{\delta\rho_{RR}\left(\rho_{SR}P_{\text{com}}+1\right)}{\lambda_{11}\left(\delta\rho_{RR}+2\eta\rho_{LI}\right)\theta'-\lambda_{12}+\lambda_{13}}}-\left(\rho_{SR}P_{\text{com}}+1\right)\right]\right)^{+}. \tag{45}$$

$$R_{\text{sum}}=\frac{1}{\ln 2}\left[\min\left(\ln\left(l_1\right)-\ln\left(f_1\right),-\ln\left(b_n\right)\right)+\ln\left(f_2\right)+\ln\left(f_3\right)-\ln\left(a_n\right)-2\ln\left(N_0\right)\right], \tag{52}$$

Algorithm 1: Alternate Optimization Algorithm

input : The maximum number of iterations L, $\ell=1$, and $\lambda>0$.

output: the optimal PA coefficients P_{sen}^{ℓ}, P_{com}^{ℓ}, a_n^{ℓ}, and b_n^{ℓ}.

Initialize P_{sen}^{1}, P_{com}^{1}, a_n^{1}, and b_n^{1} according to (39c) and (39d).
repeat
  $\ell=\ell+1$
  Fixed $a_n=a_n^{\ell-1}$, $b_n=b_n^{\ell-1}$, $P_{\text{com}}=P_{\text{com}}^{\ell-1}$, $\lambda_{11}\geqslant 0$, $\lambda_{12}\geqslant 0$, and $\lambda_{13}\geqslant 0$.
  repeat
    Set $t=1$.
    Derive the optimal λ_{11}^{*}, λ_{12}^{*}, and λ_{13}^{*} until convergence using the subgradient-based method.
    Solve (43) for given λ_{11}^{*}, λ_{12}^{*}, and λ_{13}^{*} and denote the solution as P_{sen}^{t+1}.
    Update $t=t+1$.
  until *The objective value of (43) reaches convergence*;
  Update $P_{\text{sen}}^{\ell}=P_{\text{sen}}^{t}$.
  Fixed $P_{\text{sen}}=P_{\text{sen}}^{\ell}$, update P_{com}^{ℓ} according to (44).
  Fixed $P_{\text{sen}}=P_{\text{sen}}^{\ell}$ and $P_{\text{com}}=P_{\text{com}}^{\ell}$, update a_n^{ℓ} and b_n^{ℓ} according to (46) and (47).
  Update $\ell=\ell+1$.
until $\gamma_{SR}^{R}\left(\ell\right)-\gamma_{SR}^{R}\left(\ell-1\right)\leqslant\lambda$ *or* $\ell=L$;

$l_1=\rho_{SR}+\rho_{RR}\delta+2\eta\rho_{LI}$, $f_1=a_n\rho_{SR}+\rho_{RR}\delta+2\eta\rho_{LI}$, $f_2=a_n\rho_{RD_n}P_{\text{sen}}+N_0$ and $f_3=a_n\rho_{SD_n}P_{\text{com}}+N_0$.

Substituting (7)-(12) and (40) into (51a)-(51c), after some mathematical manipulations, (51) can be rewritten as

$$\underset{P_{\text{com}},P_{\text{sen}},a_n,b_n}{\text{maximize}}\quad R_{\text{sum}} \tag{53}$$
$$\text{s.t. } a_n\rho_{SR}P_{\text{com}}-l_2\gamma_{\text{th}_n}P_{\text{sen}}-N_0\gamma_{\text{th}_n}\geqslant 0, \tag{53a}$$
$$l_3P_{\text{com}}-l_2\gamma_{\text{th}_f}P_{\text{sen}}-N_0\gamma_{\text{th}_f}\geqslant 0, \tag{53b}$$
$$l_4P_{\text{sen}}-\kappa\rho_{SR}P_{\text{com}}-\kappa N_0\geqslant 0, \tag{53c}$$
$$C_2\leqslant P_{\text{com}}\leqslant P_{\max},C_3\leqslant P_{\text{sen}}\leqslant P_{\max},\ (41\text{d}), \tag{53d}$$

where $l_2=\rho_{RR}\delta+2\eta\rho_{LI}$, $l_3=a_f\rho_{SR}-a_n\rho_{SR}\gamma_{\text{th}_f}$, $l_4=\delta\rho_{RR}-2\eta\kappa\rho_{LI}$, $C_2=\max\left(C_{21},C_{22},C_{23}\right)$ with $C_{21}=N_0\gamma_{\text{th}_f}/\left(a_f\rho_{SD_f}-a_n\rho_{SD_f}\gamma_{\text{th}_f}\right)$, $C_{22}=N_0\gamma_{\text{th}_f}/\left(a_f\rho_{SD_n}-a_n\rho_{SD_n}\gamma_{\text{th}_f}\right)$, and $C_{23}=N_0\gamma_{\text{th}_n}/(a_n\rho_{SD_n})$, $C_3=\max\left(C_{31},C_{32},C_{33}\right)$ with $C_{31}=N_0\gamma_{\text{th}_f}/\left(b_f\rho_{RD_f}-b_n\rho_{RD_f}\gamma_{\text{th}_f}\right)$, $C_{32}=N_0\gamma_{\text{th}_n}/(b_f\rho_{RD_n}-b_n\rho_{RD_n}\gamma_{\text{th}_n})$, and $C_{32}=N_0\gamma_{\text{th}_n}/(b_n\rho_{RD_n})$.

Similar to (42), it is hard to simultaneously optimize P_{com}, P_{sen}, a_n, and b_n , therefore we adopt AO to derive the PA coefficients as well. By introducing the slack variable V and according to (52), we can rewrite (53) as (54), shown at the top of the next page.

Since (54) is a convex problem, the Lagrangian function can be expressed as (55), shown at the top of the next page.

It is easy to obtain that $\lambda_{21}+\lambda_{22}=1$ and the KKT conditions are expressed as

$$\frac{\partial L}{\partial P_{\text{com}}}=\frac{\lambda_{21}a_n\rho_{SD_n}}{f_3}-\lambda_{23}\kappa\rho_{SR}+\lambda_{24}l_3+\lambda_{25}a_n\rho_{SR}-\lambda_{26}+\lambda_{28}=0, \tag{56}$$
$$\frac{\partial L}{\partial P_{\text{sen}}}=\frac{(\lambda_{21}+\lambda_{22})a_n\rho_{RD_n}}{f_2}+\lambda_{23}l_4-\lambda_{24}l_2\gamma_{\text{th}_f}-\lambda_{25}l_2\gamma_{\text{th}_n}-\lambda_{27}+\lambda_{29}=0. \tag{57}$$

Based on (56) and (57), the PA coefficients P_{com}^{*} and P_{sen}^{*} are respectively expressed as

$$P_{\text{com}}^{*}=\left[\frac{\lambda_{21}}{\lambda_{23}\kappa\rho_{SR}-\lambda_{24}l_3-\lambda_{25}a_n\rho_{SR}+\lambda_{26}-\lambda_{28}}-\frac{N_0}{a_n\rho_{SD_n}}\right]^{+}, \tag{58}$$

$$P_{\text{sen}}^{*}=\left[\frac{\lambda_{21}+\lambda_{22}}{\lambda_{24}l_2\gamma_{\text{th}_f}-\lambda_{23}l_4+\lambda_{25}l_2\gamma_{\text{th}_n}+\lambda_{27}-\lambda_{29}}-\frac{N_0}{a_n\rho_{SD_n}}\right]^{+}. \tag{59}$$

Similarly, the problem can be solved by adopting the subgradient method, and the subgradient at $(\lambda_{21},\lambda_{23},\lambda_{24},\lambda_{25},\lambda_{26},\lambda_{27},\lambda_{28},\lambda_{29})$ is written as

$$\mathbf{d}=\left[d_{21},d_{23},d_{24},d_{25},d_{26},d_{27},d_{28},d_{29}\right], \tag{60}$$

where we have $d_{21}=\ln\left(l_1\right)-\ln\left(f_1\right)+\ln\left(b_n\right)$, $d_{23}=l_4P_{\text{sen}}^{*}-\kappa\rho_{SR}P_{\text{com}}^{*}-\kappa N_0$, $d_{24}=l_3P_{\text{com}}^{*}-l_2\gamma_{\text{th}_f}P_{\text{sen}}^{*}-N_0\gamma_{\text{th}_f}$, $d_{25}=a_n\rho_{SR}P_{\text{com}}^{*}-l_2\gamma_{\text{th}_n}P_{\text{sen}}^{*}-N_0\gamma_{\text{th}_f}$, $d_{26}=P_{\max}-P_{\text{com}}^{*}$, $d_{27}=P_{\max}-P_{\text{sen}}^{*}$, $d_{28}=P_{\text{com}}^{*}-C_2$, and $d_{29}=P_{\text{sen}}^{*}-C_3$.

Next, we optimize a_n and b_n at a fixed P_{com} and P_{sen}. Substituting (7)-(12) into (53a) and (53b), after some mathematical manipulations, the PA problem can be written as

$$\underset{a_n,b_n}{\text{maximize}}\ R_{\text{sum}} \tag{61}$$
$$\text{s.t. } C_4\leqslant a_n\leqslant C_5,C_6\leqslant b_n\leqslant C_7,\ (41\text{d}), \tag{61a}$$

where $C_4=\max\left(C_{41},C_{42}\right)$, $C_{41}=(l_2P_{\text{sen}}\gamma_{\text{th}_n}+N_0\gamma_{\text{th}_n})/(\rho_{SR}P_{\text{com}})$, $C_{42}=N_0\gamma_{\text{th}_n}/(\rho_{SD_n}P_{\text{com}})$, $C_5=\min\left(C_{51},C_{52},C_{53}\right)$, $C_{51}=\left(P_{\text{com}}\rho_{SR}-l_2P_{\text{sen}}\gamma_{\text{th}_f}-N_0\gamma_{\text{th}_f}\right)/\left[P_{\text{com}}\rho_{SR}\left(1+\gamma_{\text{th}_f}\right)\right]$,

$$\underset{P_{\rm com},P_{\rm sen},V}{\text{maximize}} \quad V \tag{54}$$

$$\text{s.t. } V \leqslant \ln(l_1) - \ln(f_1) + \ln(f_2) + \ln(f_3) - \ln(a_n) - 2\ln(N_0), \tag{54a}$$

$$V \leqslant -\ln(b_n) + \ln(f_2) + \ln(f_3) - \ln(a_n) - 2\ln(N_0), (53a) - (53d). \tag{54b}$$

$$\begin{aligned} L(P_{\rm com}, P_{\rm sen}, V, \lambda_{21}, \lambda_{22}, \lambda_{23}, \lambda_{24}, \lambda_{25}, \lambda_{26}, \lambda_{27}, \lambda_{28}, \lambda_{29}) &= V + \lambda_{21}(\ln(l_1) - \ln(f_1) + \ln(f_2) + \ln(f_3) \\ &- \ln(a_n) - 2\ln(N_0) - V) + \lambda_{22}(-\ln(b_n) + \ln(f_2) + \ln(f_3) - \ln(a_n) - 2\ln(N_0) - V) \\ &+ \lambda_{23}(l_4 P_{\rm sen} - \kappa\rho_{SR}P_{\rm com} - \kappa N_0) + \lambda_{24}\left(l_3 P_{\rm com} - l_2\gamma_{{\rm th}_f}P_{\rm sen} - N_0\gamma_{{\rm th}_f}\right) + \lambda_{25}(a_n\rho_{SR}P_{\rm com} - l_2\gamma_{{\rm th}_n}P_{\rm sen} \\ &- N_0\gamma_{{\rm th}_f}) + \lambda_{26}(P_{\max} - P_{\rm com}) + \lambda_{27}(P_{\max} - P_{\rm sen}) + \lambda_{28}(P_{\rm com} - C_2) + \lambda_{29}(P_{\rm sen} - C_3). \end{aligned} \tag{55}$$

$C_{52} = g_1\left(\rho_{SD_f}\right)$, $C_{53} = g_1\left(\rho_{SD_n}\right)$, $C_6 = N_0\gamma_{{\rm th}_n}/(\rho_{RD_n}P_{\rm sen})$, $C_7 = \min(C_{71}, C_{72})$, $C_{71} = g_2\left(\rho_{RD_f}\right)$, and $C_{72} = g_2\left(\rho_{RD_n}\right)$. Then, $g_1(\rho)$ and $g_2(\rho)$ are respectively given by

$$g_1(\rho) = \frac{P_{\rm com}\rho - N_0\gamma_{{\rm th}_f}}{P_{\rm com}\rho\left(1+\gamma_{{\rm th}_f}\right)}, \tag{62}$$

$$g_2(\rho) = \frac{P_{\rm sen}\rho - N_0\gamma_{{\rm th}_f}}{P_{\rm sen}\rho\left(1+\gamma_{{\rm th}_f}\right)}. \tag{63}$$

For the sake of further analysis, $R_{\rm sum}$ is divided into two cases as (64), shown at the top of the next page.

From (64), it can be inferred that the first-order derivative of $R_{\rm sum}$ with respect of a_n in the high-SNR regime always satisfies $\partial R_{\rm sum}/\partial a_n > 0$. Furthermore, if $\ln(l_1) - \ln(f_1) \leqslant \ln\left(b_n^{-1}\right)$, we can observe that $\partial R_{\rm sum}/\partial b_n = 0$, and we can further observe that $\partial R_{\rm sum}/\partial b_n < 0$, if $\ln(l_1) - \ln(f_1) > \ln\left(b_n^{-1}\right)$. Thus, $R_{\rm sum}$ can be maximized if and only if b_n satisfies $\ln(l_1) - \ln(f_1) = \ln\left(b_n^{-1}\right)$. Therefore, the PA coefficients a_n^* and b_n^* are respectively given by

$$a_n^* = 0.5 - \sigma, \tag{65}$$

$$b_n^* = \frac{a_n^*\rho_{SR} + \rho_{RR}\delta + 2\eta\rho_{LI}}{\rho_{SR} + \rho_{RR}\delta + 2\eta\rho_{LI}}. \tag{66}$$

The alternating optimization algorithm of the CCD scheme is summarized in Algorithm 2, which iteratively determines the PA coefficients.

Remark 7. *For the CCD scheme, the computational complexity of the algorithm is $O[(K_3+1)K_4]$, where K_3 denotes the number of iterations to find the optimal Lagrangian and K_4 is the number of iterations in the main loop.*

VII. Numerical Results

In this section, some numerical results are provided for supporting the theoretical analysis presented in Section III-Section VI by using Monte-Carlo computer simulations. Hereinafter, unless otherwise mentioned, the simulation parameters are as follows: $a_f = b_f = 0.7$, $a_n = b_n = 0.3$, $\gamma_{{\rm th}_f} = 1$, $\gamma_{{\rm th}_n} = 2$, $\delta = 0.2$, $N_0 = 1$, $\Omega = 5$, $\alpha = 2$, $\eta = 0.01$, $d_{LI} = 0.5$ m $d_{SR} = 100$ m, $d_{RD_f} = 200$ m, $d_{RD_n} = 150$ m, $d_{SD_n} = 200$ m, $d_{SD_f} = 250$ m, $d_{RT} = d_{TR} = 75$ m [38]–[40].

Algorithm 2: Alternate Optimization Algorithm

input : The maximum number of iterations Ψ, $\psi = 1$, and $\dagger > 0$.

output: the optimal PA coefficients $P_{\rm sen}^{\psi}$, $P_{\rm com}^{\psi}$, a_n^{ψ}, and b_n^{ψ}.

Initialize $P_{\rm sen}^1$, $P_{\rm com}^1$, a_n^1, and b_n^1 according to (39d) and (50d).

repeat

  $\psi = \psi + 1$

  Fixed $a_n = a_n^{\psi-1}$, $b_n = b_n^{\psi-1}$, $0 \leqslant \lambda_{21} \leqslant 1$, $\lambda_{23} \geqslant 0$, $\lambda_{24} \geqslant 0$, $\lambda_{25} \geqslant 0$, $\lambda_{26} \geqslant 0$, $\lambda_{27} \geqslant 0$, $\lambda_{28} \geqslant 0$, and $\lambda_{29} \geqslant 0$.

  repeat

    Set $q = 1$.

    Derive the optimal λ_{21}^*, λ_{23}^*, λ_{24}^*, λ_{25}^*, λ_{26}^*, λ_{27}^*, λ_{28}^*, and λ_{29}^* until convergence using the subgradient-based method.

    Solve (55) for given λ_{21}^*, λ_{23}^*, λ_{24}^*, λ_{25}^*, λ_{26}^*, λ_{28}^* and denote the solution as $P_{\rm com}^{q+1}$.

    Solve (56) for given λ_{21}^*, λ_{23}^*, λ_{24}^*, λ_{25}^*, λ_{27}^*, λ_{29}^* and denote the solution as $P_{\rm sen}^{q+1}$.

    Update $q = q + 1$.

  until *The objective value of (55) and (56) reaches convergence*;

  Update $P_{\rm com}^{\psi} = P_{\rm com}^{q}$ and $P_{\rm sen}^{\psi} = P_{\rm sen}^{q}$.

  Fixed $P_{\rm com}^{\psi} = P_{\rm com}^{q}$ and $P_{\rm sen}^{\psi} = P_{\rm sen}^{q}$, update a_n^{ψ} and b_n^{ψ} according to (61) and (62).

  Update $\psi = \psi + 1$.

until $R_{\rm sum}(\psi) - R_{\rm sum}(\psi - 1) \leqslant \dagger$ *or* $\psi = \Psi$;

Fig. 2 presents the OPs of D_n and D_f versus the transmit power of S with $P_{\rm com} = P_{\rm sen}$. For comparison, the OP of the traditional non-cooperative NO-DLT and cooperative HD NO-DLT schemes are presented as well at the same power consumption. It can be seen from Fig. 2 that the Monte Carlo simulation perfectly matches the analytical results and the convergence between the curves in the high-SNR regime verifies the accuracy of the results derived in (16), (19), (21), and (22). We can also observe from Fig. 2 that the OPs of the IoT devices for the proposed FD NO-DLT ISAC scheme

$$R_{\text{sum}} = \begin{cases} \frac{1}{\ln 2}\left[\ln\left(l_1\right) - \ln\left(f_1\right) + \ln\left(f_2\right) + \ln\left(f_3\right) - \ln\left(a_n\right) - 2\ln\left(N_0\right)\right], \text{ if } \ln\left(l_1\right) - \ln\left(f_1\right) \leqslant \ln\left(b_n^{-1}\right) \\ \frac{1}{\ln 2}\left[-\ln\left(b_n\right) + \ln\left(f_2\right) + \ln\left(f_3\right) - \ln\left(a_n\right) - 2\ln\left(N_0\right)\right], \text{ if } \ln\left(l_1\right) - \ln\left(f_1\right) > \ln\left(b_n^{-1}\right) \end{cases}. \quad (64)$$

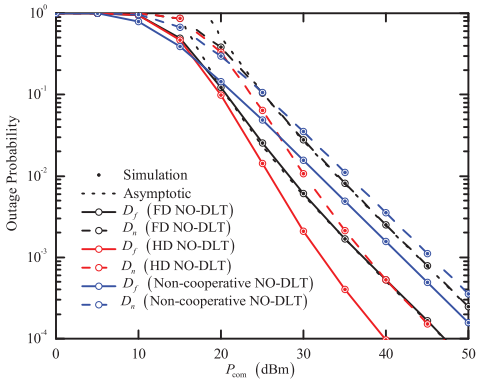

Fig. 2: OPs of the IoT devices vs. the transmit power of S.

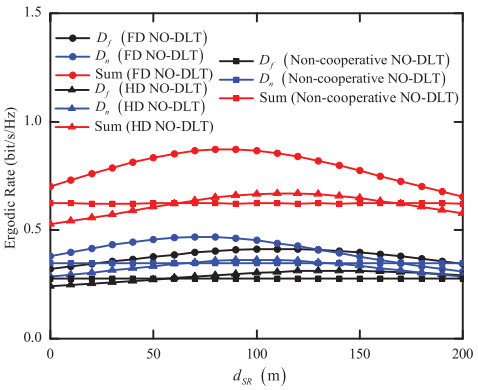

Fig. 4: ERs of the IoT devices vs. the relay location.

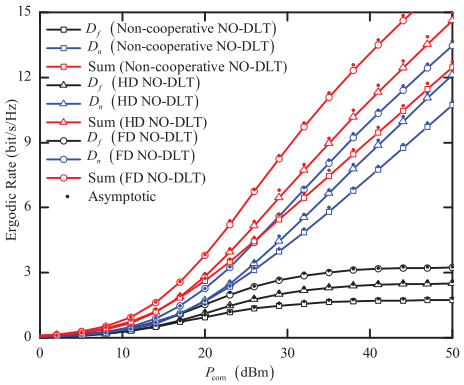

Fig. 3: ERs of the IoT devices vs. the transmit power of S.

are lower than the traditional non-cooperative NO-DLT at the same energy consumption. This is due to the fact that cooperative NO-DLT transmissions are capable of significantly improving the frequency band exploitation . Furthermore, we notice that the OP of the proposed FD NO-DLT scheme is worse than that of HD NO-DLT, mainly due to the additional CLSI.

Fig. 3 demonstrates the ERs of D_n and D_f versus the transmit power of S with $P_{\text{com}} = P_{\text{sen}}$. We reiterate that the total power consumption of the three schemes is identical to ensure a fair comparison. It can be observed from Fig. 3 that the ER of D_n keeps on increasing, while for D_f, the ER tends to be saturate eventually. In fact, the ER of the far IoT device is numerically expressed as $\log_2\left(1 + a_f/a_n\right) + \log_2\left[1 + a_f\beta_{SR}/\left(a_n\beta_{SR} + 2\beta_{RR}^2\delta + 2\eta\beta_{LI}\right)\right]$ for the FD NO-DLT, $\log_2\left(1 + a_f/a_n\right) + 0.5\log_2\left[1 + a_f\beta_{SR}/\left(a_n\beta_{SR} + 2\beta_{RR}^2\delta + 2\eta\beta_{LI}\right)\right]$ for the HD NO-DLT, and $\log_2\left(1 + a_f/a_n\right)$ for the non-cooperative NO-DLT in the high SNR regime. Moreover, it can be seen that the ER of the near IoT device would eventually govern the ESR in the high-SNR regime.

Fig. 4 illustrates the ERs of D_n and D_f versus the relay location for the FD, HD, and non-cooperative schemes. Since the near IoT device makes a significant contribution to the ESR, for tangibly characterizing the system performance, we assume that S, R, and D_n are positioned along a straight line, and R is located between S and D_n. We set $P_{\text{com}} = P_{\text{sen}} = 20$ dBm, $d_{SD_n} = 200$ m, $d_{SD_f} = 250$ m, the angle between $S \to D_f$ and $S \to D_n$ is set to $\phi = 30°$, thus the distance between R and D_f is $d_{RD_f} = \sqrt{d_{SR}^2 + d_{SD_f}^2 - 2d_{SR}d_{SD_f}\cos\phi}$. Observe from Fig. 4 that for the cooperative NO-DLT schemes, the ESR of the IoT devices improves first and then degrades upon increasing d_{SR}. The reason for this phenomenon can be attributed to the fact that the increase of d_{SR} improves the channel gains between the relay and the IoT devices. However, at a shorter d_{RD_n}, the path loss between the MaBS and the relay increases, thus degrading the data transmission. Additionally, it can also be seen that if R and D_n are particularly close to each other, the ERs of D_n for the FD and HD NO-DLT become inferior to that of non-cooperative NO-DLT, since the cooperative NO-DLT schemes have to share a portion of the total power for target sensing.

Fig. 5 shows the PoD of the MiBS versus the transmit power of R at $\text{P}_{\text{fa}} = 10^{-5}$. Intuitively, the PoD can be improved by increasing the transmit power of R. It can be observed that the PoD of the proposed NO-DLT ISAC system is superior to that of the traditional O-DLT, since NO-DLT can serve multiple IoT devices at the same time, whereas O-DLT requires repeated communication signal transmission, which further increases the interference during sensing. We can further see from Fig. 5 that the sensing behavior can be improved by reducing P_{com}, which is due to the fact that the

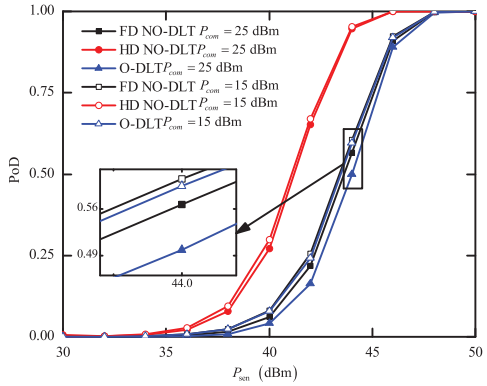

Fig. 5: PoD vs. the transmit power of the MiBS.

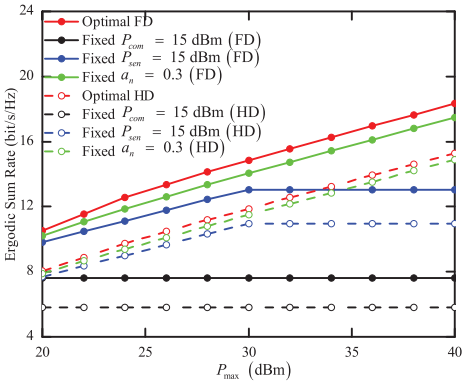

Fig. 7: Sum rate vs. the maximum power budget of the MaBS and MiBS.

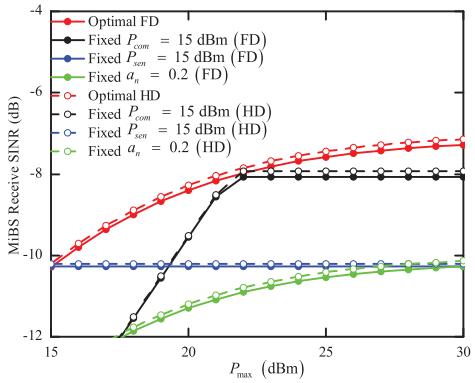

Fig. 6: Receive SINR of x_r vs. the maximum power budget of the MaBS and MiBS.

signal transmitted by the MaBS is regarded as interference. Furthermore, due to the existence of supererogatory CLSI, the sensing performance of FD NO-DLT scheme lags behind that of HD NO-DLT at the same parameter settings, which is consistent with the result of (35).

Fig. 6 plots the receive SINR of x_r at the MiBS versus the power budget of the MaBS and the MiBS $P_{\max}$ for both the FD and HD modes. For comparison, we plot the curves of the proposed PA scheme and three other random power allocation (RPA) baseline schemes, i.e., *1)* Jointly optimizing P_{sen}, a_n, and b_n at fixed P_{com} = 15 dBm; *2)* Jointly optimizing P_{com}, a_n, and b_n at fixed P_{sen} = 15 dBm; *3)* Jointly optimizing P_{com} and P_{sen} at fixed $a_n = b_n$ = 0.2. For a fixed P_{com}, the receive SINR of x_r first increases with $P_{\max}$ and then gradually saturating with a diminishing small return for an exceedingly large $P_{\max}$. This is because the increase of $P_{\max}$ also increases P_{sen} and further improves the receive SINR of x_r. However, if the critical communication decoding capability is reached, no additional sensing power is allocated so as to cater for the lowest signals decoding of communication, and the receive SINR of x_r remains unchanged. For a fixed P_{sen}, the sensing performance is degraded as P_{com} increases, once the required decoding requirements are achieved, the receive SINR of x_r saturates. For the fixed a_n and b_n, limited by the decoding requirements, the receive SINR of x_r observed for the RPA scheme lags behind that of the proposed PA scheme. Additionally, it can be observed from Fig. 6 that due to the existence of CLSI, the receive SINR of the FD mode becomes lower than that of the HD mode.

Fig. 7 shows the advantages of the proposed PA scheme over other RPA baseline schemes in terms of the sum rate attained in both the FD and HD modes. As seen from Fig. 7, the proposed PA scheme is superior to the schemes of the fixed P_{com}, P_{sen} or a_n. For a fixed P_{com}, due to associated the sensing constraint and the requirements of communication signals decoding, the sum rate remains constant. Furthermore, for a given P_{sen}, the sum rate increases with $P_{\max}$. This phenomenon continues until the communication scheme reaches its peak power at a fixed sensing demand. For the fixed a_n and b_n, restricted by the characteristics of the objective function and the decoding of communication signals, the sum rate becomes inferior to that of the proposed PA scheme. Finally, as expected, the sum rate of the FD NO-DLT system considered is reduced by the CLSI compared to that of the HD mode.

VIII. Conclusion

In this paper, we studied a FD NO-DLT ISAC system, in which the MiBS supports simultaneous target sensing and cooperative relaying. We characterized the performance of C&S by deriving both the exact and asymptotic OPs, the diversity orders, the approximate ESR expressions for communication, the PoFA and PoD as well as the velocity and distance between the MiBS and target for sensing. To further characterize the performance of the system considered, both the SCD and CCD, PA problems were solved. Then, the maximization problems of the sensing signal's receive SINR at the MiBS and the IoT devices' sum rate were determined by using the Lagrangian method. The simulation results demonstrated that the FD NO-DLT system outperformed its traditional non-cooperative counterpart in terms of its OP at a constant total power, while it was inferior to the HD NO-DLT system. In

terms of the ESR, the location of the MiBS had a substantial influence on it and the FD NO-DLT revealed its benefits. Furthermore, the sensing performance of the proposed FD NO-DLT ISAC system is improved over that of the traditional O-DLT scheme as well. Finally, we confirmed that the proposed PA scheme is superior to the RPA schemes.

Appendix A: Proof of Theorem 1

Upon substituting (9) and (10) into (15), I_1 can be rewritten as (A.1), shown at the top of the next page.

By using PDFs and CDFs of ρ_i, $I_{1,\mathrm{I}}$ can be expressed as

$$I_{1,\mathrm{I}} = 1 - \frac{\beta_{SR}}{2\beta_{RR}\left(\beta_{SR}+2\eta\beta_{LI}\gamma_r\theta_1\right)} e^{-\frac{\theta_1}{\beta_{SR}}} \times \underbrace{\int_0^{\infty} \frac{1}{\sqrt{x}} e^{-\frac{\sqrt{x}}{\beta_{RR}} - \frac{x\delta\gamma_r\theta_1}{\beta_{SR}}} dx}_{I_{1,\mathrm{I}}^{\Delta}}. \tag{A.2}$$

By defining $t \triangleq \sqrt{x}$ and using [51, Eq. (3.322.2)], $I_{1,\mathrm{I}}^{\Delta}$ can be further expressed as

$$\begin{aligned} I_{1,\mathrm{I}}^{\Delta} &= 2\int_0^{\infty} e^{-\frac{t}{\beta_{RR}} - \frac{\delta\gamma_r\theta_1 t^2}{\beta_{SR}}} dt \\ &= \sqrt{\frac{\pi\beta_{SR}}{\delta\gamma_r\theta_1}} e^{\frac{\beta_{SR}}{4\beta_{RR}^2\delta\gamma_r\theta_1}} \left[1 - \mathrm{erfc}\left(\frac{1}{2\beta_{RR}}\sqrt{\frac{\beta_{SR}}{\delta\gamma_r\theta_1}}\right)\right]. \end{aligned} \tag{A.3}$$

Substituting the PDF of ρ_i into the second part of (A.1), after some straightforward mathematical manipulations, I_1 can be finally expressed as

$$\begin{aligned} I_1 = &\left(1 - e^{-\frac{\theta_1}{\beta_{SD_f}}}\right)\Bigg\{1 - \frac{\beta_{SR}}{2\beta_{RR}\left(\beta_{SR}+2\eta\beta_{LI}\gamma_r\theta_1\right)} e^{\frac{\beta_{SR}}{4\beta_{RR}^2\delta\gamma_r\theta_1} - \frac{\theta_1}{\beta_{SR}}} \\ &\times\sqrt{\frac{\pi\beta_{SR}}{\delta\gamma_r\theta_1}}\left[1 - erfc\left(\frac{1}{2\beta_{RR}}\sqrt{\frac{\beta_{SR}}{\delta\gamma_r\theta_1}}\right)\right]\Bigg\}. \end{aligned} \tag{A.4}$$

Upon substituting (9), (10), and (12) into (15), and similar to I_1, after some mathematical manipulations, I_2 can be expressed as

$$\begin{aligned} I_2 = &\left(1 - e^{-\frac{\theta_1}{\beta_{SD_f}}}\right)\left(1 - e^{-\frac{\varphi_1}{\beta_{RD_f}}}\right) \frac{\beta_{SR}}{2\beta_{RR}\left(\beta_{SR}+2\eta\beta_{LI}\gamma_r\theta_1\right)} \\ &\times e^{\frac{\beta_{SR}}{4\beta_{RR}^2\delta\gamma_r\theta_1} - \frac{\theta_1}{\beta_{SR}}} \sqrt{\frac{\pi\beta_{SR}}{\delta\gamma_r\theta_1}}\left[1 - \mathrm{erfc}\left(\frac{1}{2\beta_{RR}}\sqrt{\frac{\beta_{SR}}{\delta\gamma_r\theta_1}}\right)\right]. \end{aligned} \tag{A.5}$$

Substituting (A.4) and (A.5) into (15), after some straightforward mathematical manipulations, (16) can be obtained.

Appendix B: Proof of Corollary 1

In the high-SNR regime of $\gamma_c, \gamma_r \to \infty$, we can obtain

$$\lim_{\gamma_c\to\infty} \theta_1 = \lim_{\gamma_c\to\infty} \frac{\gamma_{\mathrm{th}_f}}{a_f\gamma_c - a_n\gamma_c\gamma_{\mathrm{th}_f}} \approx 0, \tag{B.1}$$

$$\lim_{\gamma_r\to\infty} \varphi_1 = \lim_{\gamma_r\to\infty} \frac{\gamma_{\mathrm{th}_f}}{a_f\gamma_r - a_n\gamma_r\gamma_{\mathrm{th}_f}} \approx 0, \tag{B.2}$$

$$\lim_{\gamma_c,\gamma_r\to\infty} \gamma_r\theta_1 = \lim_{\gamma_r\to\infty} \frac{\gamma_r\gamma_{\mathrm{th}_f}}{a_f\gamma_c - a_n\gamma_c\gamma_{\mathrm{th}_f}} \approx \theta_1^*. \tag{B.3}$$

Upon substituting (B.3) into (A.1), $I_{1,\mathrm{I}}$ can be expressed as in the high-SNR regime

$$I_{1,\mathrm{I}}^{\infty} = \int_0^{\infty}\int_0^{\infty}\int_0^{x\delta\theta_1^*+2y\theta_1^*} f_{\rho_{RR}}(x) f_{\rho_{LI}}(y) f_{\rho_{SR}}(z)\, dxdydz. \tag{B.4}$$

Similar to (A.2), after some mathematical manipulations, we can obtain the expression of $I_{1,\mathrm{I}}^{\infty}$.

When $x \to 0$, the approximation $1 - e^x \approx x$ holds and substituting (B.1) into (A.1), $I_{1,\mathrm{II}}$ in the high SNR regime is expressed as $I_{1,\mathrm{II}}^{\infty} = \theta_1/\beta_{SD_f}$.

Likewise, we can obtain I_2^{∞} by using the same method. Substituting I_1^{∞} and I_2^{∞} into (15), (21) can be obtained.

Appendix C: Proof of Theorem 3

Upon defining $W_1 \triangleq \min\left(\gamma_{SR}^{D_f}, \gamma_{RD_f}^{D_f}, \gamma_{RD_n}^{D_f}\right)$ and $W_2 \triangleq \min\left(\gamma_{SD_f}^{D_f}, \gamma_{SD_n}^{D_f}\right)$, the achievable rate of D_f can be rewritten as

$$R_f = \underbrace{\log_2(1+W_1)}_{R_f^1} + \underbrace{\log_2(1+W_2)}_{R_f^2}. \tag{C.1}$$

Substituting (10), (12), and (13) into W_1, with the aid of probability theory, the CDF of W_1 can be expressed as

$$\begin{aligned} F_{W_1}(w_1) &= 1 - \Pr\Bigg(\rho_{SR} \geqslant \frac{\delta\gamma_r\rho_{RR}}{g_c(w_1)} + \frac{2\eta\gamma_r\rho_{LI}}{g_c(w_1)} + \frac{1}{g_c(w_1)} \\ &\qquad \rho_{RD_f} \geqslant g_r(w_1), \rho_{RD_n} \geqslant g_r(w_1)\Bigg) \\ &= 1 - \frac{\beta_{SR}g_c(w_1)}{2\beta_{RR}\left(\beta_{SR}g_c(w_1)+2\beta_{LI}\gamma_r\right)} \sqrt{\frac{\pi\beta_{SR}g_c(w_1)}{\delta\gamma_r}} \\ &\quad \times e^{\frac{\beta_{SR}g_c(w_1)}{4\beta_{RR}^2\delta\gamma_r} - \frac{1}{\beta_{SR}g_c(w_1)} - \frac{1}{\beta_{RD_f}g_r(w_1)} - \frac{1}{\beta_{RD_n}g_r(w_1)}} \\ &\quad \times \left[1 - \mathrm{erfc}\left(\frac{1}{2\beta_{RR}}\sqrt{\frac{g_c(w_1)\beta_{SR}}{\delta\gamma_r}}\right)\right]. \end{aligned} \tag{C.2}$$

Next, we can further observe that

$$\begin{aligned} R_{\mathrm{ave}}^{f,1} &= \int_0^{\infty} \log_2(1+w_1) f_{W_1}(w_1) dw_1 \\ &= \frac{1}{\ln 2}\int_0^{\infty} \frac{1 - F_{W_1}(w_1)}{1+w_1} dw_1. \end{aligned} \tag{C.3}$$

Substituting (C.2) into (C.3), we can obtain the expression of $R_{\mathrm{ave}}^{f,1}$. The same procedure can be adopted for the proof of $R_{\mathrm{ave}}^{f,2}$. Then, we can obtain (27) after some mathematical manipulations.

Likewise, we can derive $R_{\mathrm{ave}}^{n,1}$ following the same approach as in (C.2).

For $R_{\mathrm{ave}}^{n,2}$, denoting $U \triangleq \gamma_{SD_n}^{D_n}$ first, the CDF of U can be written as

$$F_U(u) = \Pr\left(a_n\rho_{SD_n}\gamma_c \leqslant u\right) = 1 - e^{-\frac{u}{\beta_{SD_n}a_n\gamma_c}}. \tag{C.4}$$

Similar to (C.3), and with the aid of [51, Eq. (3.352.4)], the exact expression of $R_{\mathrm{ave}}^{n,2}$ can be formulated as

$$R_{\mathrm{ave}}^{n,2} = -\frac{1}{\ln 2} e^{\frac{1}{\beta_{SD_n}a_n\gamma_c}} \mathrm{Ei}\left(-\frac{1}{\beta_{SD_n}a_n\gamma_c}\right). \tag{C.5}$$

After some straightforward mathematical manipulations, (28) can be obtained.

$$
\begin{aligned}
I_1 &= \Pr\left(\frac{a_f \rho_{SR}\gamma_c}{a_n \rho_{SR}\gamma_c + \rho_{RR}\delta\gamma_r + 2\eta\rho_{LI}\gamma_r + 1} < \gamma_{\mathrm{th}_f}\right) \Pr\left(\frac{a_f \rho_{SD_f}\gamma_c}{a_n \rho_{SD_f}\gamma_c + 1} < \gamma_{\mathrm{th}_f}\right) \\
&= \Pr\left(\rho_{SR} < \rho_{RR}\delta\gamma_r\theta_1 + 2\eta\rho_{LI}\gamma_r\theta_1 + \theta_1\right) \Pr\left(\rho_{SD_f} < \theta_1\right) \\
&= \underbrace{\int_0^\infty \int_0^\infty \int_0^{\theta_1(x\delta\gamma_r + 2y\gamma_r + 1)} f_{\rho_{SR}}(x)\, f_{\rho_{LI}}(y)\, f_{\rho_{RR}}(z)\, dxdydz}_{I_{1,\mathrm{I}}} \underbrace{\int_0^{\theta_1} f_{\rho_{SD_f}}(w) dw}_{I_{1,\mathrm{II}}}. \qquad \text{(A.1)}
\end{aligned}
$$

Appendix D: Proof of Corollary 3

Substituting (10), (12), and (13) into (23), and using the inequality [39]

$$
\mathbb{E}\left[\log_2\left(1 + \frac{x}{y}\right)\right] \approx \log_2\left(1 + \frac{\mathbb{E}[x]}{\mathbb{E}[y]}\right), \qquad \text{(D.1)}
$$

$R_{\mathrm{ave}}^{f,1}$ can be approximated as (D.3), shown at the top of the next page, where $\mathbb{E}[\rho_{SR}]$ is expressed as

$$
\mathbb{E}[\rho_{SR}] = \int_0^\infty x f_{\rho_{SR}}(x) dx = \beta_{SR}. \qquad \text{(D.2)}
$$

Then, we can obtain $\mathbb{E}\left[\rho_{RD_f}\right]$, $\mathbb{E}[\rho_{RD_n}]$, $\mathbb{E}[\rho_{RR}]$, and $\mathbb{E}[\rho_{LI}]$ with the same method. $R_{\mathrm{ave}}^{ap,f1}$ can be obtained after some mathematical manipulations.

Similarly, $R_{\mathrm{ave}}^{ap,f2}$, $R_{ave}^{ap,n1}$, and $R_{ave}^{ap,n2}$ can be derived. Then, the approximate ESR of the IoT devices can be obtained.

References

[1] F. Liu, C. Masouros, A. P. Petropulu, H. Griffiths, and L. Hanzo, "Joint radar and communication design: Applications, state-of-the-art, and the road ahead," *IEEE Trans. Commun.*, vol. 68, no. 6, pp. 3834–3862, Jun. 2020.

[2] H. Hong, J. Zhao, T. Hong, and T. Tang, "Radar-communication integration for 6G massive IoT services," *IEEE Internet Things J.*, pp. 1–11, Mar. 2021.

[3] A. Hassanien, M. G. Amin, E. Aboutanios, and B. Himed, "Dual-function radar communication systems: A solution to the spectrum congestion problem," *IEEE Signal Process. Mag.*, vol. 36, no. 5, pp. 115–126, Sept. 2019.

[4] F. Wang and H. Li, "Joint power allocation for multicarrier radar and communication coexistence," *2020 IEEE International Radar Conf. (RADAR)*, pp. 141–145, Jun. 2020.

[5] T. Wild, V. Braun, and H. Viswanathan, "Joint design of communication and sensing for beyond 5G and 6G systems," *IEEE Access*, vol. 9, pp. 30 845–30 857, Feb. 2021.

[6] F. Liu, C. Masouros, A. Li, H. Sun, and L. Hanzo, "MU-MIMO communications with MIMO radar: From co-existence to joint transmission," *IEEE Trans. Wireless Commun.*, vol. 17, no. 4, pp. 2755–2770, 2018.

[7] N. Chen and M. Okada, "Toward 6G Internet of Things and the convergence with RoF system," *IEEE Internet Things J.*, vol. 8, no. 11, pp. 8719–8733, Jun. 2021.

[8] F. Liu, Y. Cui, C. Masouros, J. Xu, T. X. Han, Y. C. Eldar, and S. Buzzi, "Integrated sensing and communications: Toward dual-functional wireless networks for 6G and beyond," *IEEE J. Sel. Areas Commun.*, vol. 40, no. 6, pp. 1728–1767, Jun. 2022.

[9] L. Chettri and R. Bera, "A comprehensive survey on Internet of Things (IoT) toward 5G wireless systems," *IEEE Internet Things J.*, vol. 7, no. 1, pp. 16–32, Jan. 2020.

[10] Q. Zhang, H. Sun, Z. Wei, and Z. Feng, "Sensing and communication integrated system for autonomous driving vehicles," *IEEE INFOCOM 2020 - IEEE Conf. Comp. Commun. Workshops (INFOCOM WKSHPS)*, pp. 1278–1279, Aug. 2020.

[11] X. Chen, Z. Feng, Z. Wei, F. Gao, and X. Yuan, "Performance of joint sensing-communication cooperative sensing UAV network," *IEEE Trans. Veh. Technol.*, vol. 69, no. 12, pp. 15 545–15 556, Dec. 2020.

[12] Z. Ding, P. Fan, and H. V. Poor, "Impact of user pairing on 5G nonorthogonal multiple-access downlink transmissions," *IEEE Trans. Veh. Technol.*, vol. 65, no. 8, pp. 6010–6023, Sept. 2016.

[13] X. Chen, R. Jia, and D. W. K. Ng, "On the design of massive non-orthogonal multiple access with imperfect successive interference cancellation," *IEEE Trans. Commun.*, vol. 67, no. 3, pp. 2539–2551, Mar. 2019.

[14] Y. Liu, S. Zhang, X. Mu, Z. Ding, R. Schober, N. Al-Dhahir, E. Hossain, and X. Shen, "Evolution of NOMA toward next generation multiple access (NGMA) for 6G," *IEEE J. Sel. Areas Commun.*, vol. 40, no. 4, pp. 1037–1071, Apr. 2022.

[15] M. Vaezi, Z. Ding, and H. V. Poor, *Multiple Access Techniques for 5G Wireless Networks and Beyond*. Eds. Cham, Switzerland: Springer, 2019.

[16] M. Sun, X. Xu, X. Tao, P. Zhang, and V. C. M. Leung, "NOMA-based D2D-enabled traffic offloading for 5G and beyond networks employing licensed and unlicensed access," *IEEE Trans. Wireless Commun.*, vol. 19, no. 6, pp. 4109–4124, Jun. 2020.

[17] H. Li, J. Li, M. Liu, Z. Ding, and F. Gong, "Energy harvesting and resource allocation for cache-enabled UAV based IoT NOMA networks," *IEEE Trans. Veh. Technol.*, vol. 70, no. 9, pp. 9625–9630, Sept. 2021.

[18] X. Chen, R. Jia, and D. W. K. Ng, "The application of relay to massive non-orthogonal multiple access," *IEEE Trans. Commun.*, vol. 66, no. 11, pp. 5168–5180, Nov. 2018.

[19] L. Bariah, S. Muhaidat, P. C. Sofotasios, F. E. Bouanani, O. A. Dobre, and W. Hamouda, "Large intelligent surface-assisted nonorthogonal multiple access for 6G networks: Performance analysis," *IEEE Internet Things J.*, vol. 8, no. 7, pp. 5129–5140, Apr. 2021.

[20] X. Li, J. Li, Y. Liu, Z. Ding, and A. Nallanathan, "Residual transceiver hardware impairments on cooperative NOMA networks," *IEEE Trans. Wireless Commun.*, vol. 19, no. 1, pp. 680–695, Jan. 2020.

[21] L. Zhang, J. Liu, M. Xiao, G. Wu, Y.-C. Liang, and S. Li, "Performance analysis and optimization in downlink NOMA systems with cooperative full-duplex relaying," *IEEE J. Sel. Areas Commun.*, vol. 35, no. 10, pp. 2398–2412, Oct. 2017.

[22] T. Riihonen, S. Werner, and R. Wichman, "Mitigation of loopback self-interference in full-duplex MIMO relays," *IEEE Trans. Signal Process.*, vol. 59, no. 12, pp. 5983–5993, Dec. 2011.

[23] D. Zhang, Y. Liu, L. Dai, A. K. Bashir, A. Nallanathan, and B. Shim, "Performance analysis of FD-NOMA-based decentralized V2X systems," *IEEE Trans. Commun.*, vol. 67, no. 7, pp. 5024–5036, Jul. 2019.

[24] Y. Sun, D. W. K. Ng, Z. Ding, and R. Schober, "Optimal joint power and subcarrier allocation for full-duplex multicarrier non-orthogonal multiple access systems," *IEEE Trans. Commun.*, vol. 65, no. 3, pp. 1077–1091, Mar. 2017.

[25] A. R. Chiriyath, B. Paul, G. M. Jacyna, and D. W. Bliss, "Inner bounds on performance of radar and communications co-existence," *IEEE Trans. Signal Process.*, vol. 64, no. 2, pp. 464–474, Jan. 2016.

[26] A. R. Chiriyath, B. Paul, and D. W. Bliss, "Radar-communications convergence: Coexistence, cooperation, and co-design," *IEEE Trans. Cogn. Commun. Netw.*, vol. 3, no. 1, pp. 1–12, Mar. 2017.

[27] F. Wang and H. Li, "Joint power allocation for radar and communication co-existence," *IEEE Signal Process. Lett.*, vol. 26, no. 11, pp. 1608–1612, Nov. 2019.

[28] F. Wang, H. Li, and M. A. Govoni, "Power allocation and co-design of multicarrier communication and radar systems for spectral coexistence," *IEEE Trans. Signal Process.*, vol. 67, no. 14, pp. 3818–3831, Jul. 2019.

[29] W. Xu, X. Li, C.-H. Lee, M. Pan, and Z. Feng, "Joint sensing duration adaptation, user matching, and power allocation for cognitive OFDM-NOMA systems," *IEEE Trans. Wireless Commun.*, vol. 17, no. 2, pp. 1269–1282, Feb. 2018.

[30] X. Liu and X. Zhang, "NOMA-based resource allocation for cluster-

$$R_{\text{ave}}^{ap,f1} \approx \frac{1}{\ln 2} \ln \left[1 + \min \left(\frac{a_f \mathbb{E}\left[\rho_{RD_f}\right] \gamma_r}{a_n \mathbb{E}\left[\rho_{RD_f}\right] \gamma_r + 1}, \frac{a_f \mathbb{E}\left[\rho_{RD_n}\right] \gamma_r}{a_n \mathbb{E}\left[\rho_{RD_n}\right] \gamma_r + 1}, \frac{a_f \mathbb{E}\left[\rho_{SR}\right] \gamma_c}{a_n \mathbb{E}\left[\rho_{SR}\right] \gamma_c + \mathbb{E}\left[\rho_{RR}\right] \delta \gamma_r + 2\eta \mathbb{E}\left[\rho_{LI}\right] \gamma_r + 1} \right) \right]. \tag{D.3}$$

based cognitive industrial internet of things," *IEEE Trans. Ind. Informat.*, vol. 16, no. 8, pp. 5379–5388, Aug. 2020.

[31] Q. Qi, X. Chen, C. Zhong, and Z. Zhang, "Integrated sensing, computation and communication in B5G cellular Internet of Things," *IEEE Trans. Wireless Commun.*, vol. 20, no. 1, pp. 332–344, Jan. 2021.

[32] A. R. Chiriyath and D. W. Bliss, "Joint radar-communications performance bounds: Data versus estimation information rates," *MILCOM 2015 - 2015 IEEE Military Commun. Conf.*, pp. 1491–1496, Oct. 2015.

[33] A. R. Chiriyath, B. Paul, and D. W. Bliss, "Simultaneous radar detection and communications performance with clutter mitigation," *2017 IEEE Radar Conf. (RadarConf)*, pp. 279–284, Jun. 2017.

[34] Z. Xiao and Y. Zeng, "Waveform design and performance analysis for full-duplex integrated sensing and communication," *IEEE J. Sel. Areas Commun.*, vol. 40, no. 6, pp. 1823–1837, Jun. 2022.

[35] Z. Wang, Y. Liu, X. Mu, Z. Ding, and O. A. Dobre, "NOMA empowered integrated sensing and communication," *IEEE Commun. Lett.*, vol. 26, no. 3, pp. 677–681, Jan. 2022.

[36] C. Ouyang, Y. Liu, and H. Yang, "On the performance of uplink ISAC systems," *IEEE Commun. Lett.*, pp. 1–5, May 2022.

[37] X. Li, Q. Wang, M. Liu, J. Li, H. Peng, M. J. Piran, and L. Li, "Cooperative wireless-powered NOMA relaying for B5G IoT networks with hardware impairments and channel estimation errors," *IEEE Internet Things J.*, vol. 8, no. 7, pp. 5453–5467, Apr. 2021.

[38] X. Yue, Y. Liu, S. Kang, A. Nallanathan, and Z. Ding, "Spatially random relay selection for full/half-duplex cooperative NOMA networks," *IEEE Trans. Commun.*, vol. 66, no. 8, pp. 3294–3308, Aug. 2018.

[39] X. Li, M. Liu, C. Deng, P. T. Mathiopoulos, Z. Ding, and Y. Liu, "Full-duplex cooperative NOMA relaying systems with I/Q imbalance and imperfect SIC," *IEEE Wireless Commun. Lett.*, vol. 9, no. 1, pp. 17–20, Jan. 2020.

[40] T. M. Hoang, L. T. Dung, B. C. Nguyen, X. N. Tran, and T. Kim, "Secrecy outage performance of FD-NOMA relay system with multiple non-colluding eavesdroppers," *IEEE Trans. Veh. Technol.*, vol. 70, no. 12, pp. 12 985–12 997, Oct. 2021.

[41] V. Liu, A. Parks, V. Talla, S. Gollakota, D. Wetherall, and J. R. Smith, "Ambient backscatter: Wireless communication out of thin air," *ACM SIGCOMM Comput. Commun. Rev.*, vol. 43, no. 4, pp. 39–50, Sept. 2013.

[42] A. Jee, K. Agrawal, and S. Prakriya, "A coordinated direct AF/DF relay-aided NOMA framework for low outage," *IEEE Trans. Commun.*, vol. 70, no. 3, pp. 1559–1579, Mar. 2022.

[43] L. Yuan, N. Yang, F. Fang, Q. Du, and Z. Zheng, "Optimal power allocation for finite blocklength cooperative NOMA with coordinated direct and relay transmission," *IEEE Wireless Commun. Lett.*, vol. 11, no. 3, pp. 523–527, Mar. 2022.

[44] H. Liu, Z. Ding, K. J. Kim, K. S. Kwak, and H. V. Poor, "Decode-and-forward relaying for cooperative NOMA systems with direct links," *IEEE Trans. Wireless Commun.*, vol. 17, no. 12, pp. 8077–8093, Dec. 2018.

[45] X. Li, M. Liu, D. Deng, J. Li, C. Deng, and Q. Yu, "Power beacon assisted wireless power cooperative relaying using NOMA with hardware impairments and imperfect CSI," *AEU - International J. Electron. Commun.*, vol. 108, pp. 275–286, Aug. 2019.

[46] M. A. Richards, J. A. Sheer, and W. A. Holm, *Principles of Modern Radar: Basic Principles*. Raleigh, North Carolina: SciTech Publishing, 2010.

[47] Z. Zhang, B. Chen, and M. Yang, "Moving target detection based on time reversal in a multipath environment," *IEEE Trans. Aerosp. Electron. Syst.*, vol. 57, no. 5, pp. 3221–3236, Apr. 2021.

[48] D. W. Bliss and S. Govindasamy, *Adaptive Wireless Communications: MIMO Channels and Networks*. New York, New York: Cambridge University Press, 2013.

[49] M. A. Richards, *Fundamentals of Radar Signal Processing*. New York, New York: McGraw-Hill, 2005.

[50] O. Abbasi, H. Yanikomeroglu, A. Ebrahimi, and N. M. Yamchi, "Trajectory design and power allocation for drone-assisted NR-V2X network with dynamic NOMA/OMA," *IEEE Trans. Wireless Commun.*, vol. 19, no. 11, pp. 7153–7168, Nov. 2020.

[51] I. S. Gradshteyn and I. M. Ryzhik, *Table of Integrals, Series, and Products, 7th ed.* New York, NY, USA: Academic, 2007.